Novel Multicomponent Crystal Forms of Artesunate

Shadrack J. Madu[1], Ke Wang[1], László Fábián[2*], and Mingzhong Li[1*]

[1]School of Pharmacy, De Montfort University, Leicester LE1 9BH, U.K.

[2]School of Chemistry, Pharmacy and Pharmacology, University of East Anglia, Norwich Research Park, Norwich NR4 7TJ, U.K.

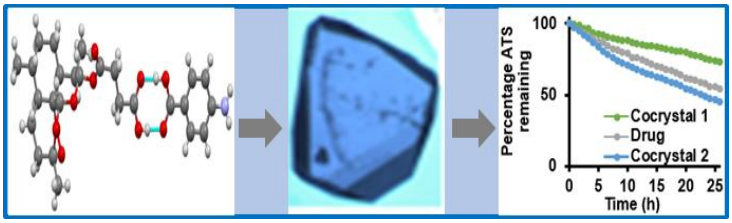
Abstract:

Artesunate (ATS), a BCS class II drug widely used for anti-malaria therapy, exhibits not only poor solubility but also poor stability. This study aimed to discover novel multicomponent crystal forms of ATS with improved physicochemical properties. Screening of 117 coformer candidates using mechanochemical solvent drop grinding (SDG) or solvent evaporation (SE) resulted in discovering five novel multicomponent crystal forms of ATS with 4-aminobenzoic acid (ABA), 1,4-diazabicyclo [2.2.2]octane (DABCO), 1,2-di(pyridine-4-yl)ethane (DPE), 1,10-phenanthroline (PHEN) and urea (URE). Based on the ΔpKa rule, FTIR results and structure analyses, these solids are cocrystals except DABCO. Additionally, ATS-URE cocrystals can be crystallised as different solvate forms, including methanol, ethanol, and acetonitrile. Interestingly two crystal forms of 2:1 ATS-DABCO have been discovered, i.e., Form 1 is cocrystal and Form 2 is salt. The crystal structures of these multicomponent ATS crystals were determined by single crystal X-ray diffraction and characterised by powder X-ray diffraction, Fourier transform infrared spectroscopy and different thermal analytical techniques (i.e., differential scanning calorimetry, thermogravimetric analysis and hot stage microscopy). It has been shown that some of the multicomponent ATS crystals can significantly improve the *in vitro* dissolution performance of ATS and its stability in solution. Unfortunately, the solid-state stability study shows that these multicomponent crystals do not exhibit better stability than the raw ATS under the conditions studied. In conclusion, the discovery of more multicomponent crystals of ATS with improved physiochemical properties (e.g., solubility and/or stability) could help to enhance its therapeutic efficacy.

Keywords: Artesunate, Dihydroartemisinin, Multicomponent cocrystal and salt, Stability

* Corresponding authors: Prof. Mingzhong Li, email: mli@dmu.ac.uk; Dr. László Fábián, email: l.fabian@uea.ac.uk

Table of Contents Graphic



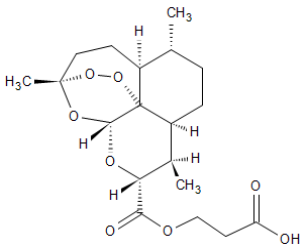
Novel multicomponent crystal forms of artesunate with improved physiochemical properties were discovered to enhance its -stability.

1. Introduction

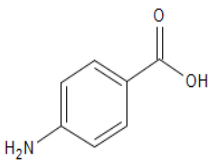
Malaria is the deadliest parasitic illness globally, with more than 600,000 mortalities annually [1]. Currently, artesunate (ATS) has been widely used in combination with other selected active antimalarial drugs (e.g., amodiaquine, sulfadoxine-pyrimethamine, mefloquine, or pyronaridine) in treating malaria [2-5]. ATS, known as dihydroartemisinin-12-α-succinate [$C_{19}H_{28}O_8$ in Figure 1(a)] and a semisynthetic artemisinin compound, can be administrated as an oral drug, a rectal suppository and intravenous and intramuscular injections [6]. Although ATS has better absorption and pharmacokinetics than its parent drug of artemisinin, it is limited by its short half-life *in vivo* and poor water solubility classified as BCS class II [7-9]; thus, a long-term repeated administration is needed for complete cure, resulting in toxicity and drug resistance [10]. Additionally, ATS is less stable and can be decomposed easily into dihydroartemisinin (DHA) at elevated temperatures, on exposure to acidic or basic environments, moisture, and light [5,11-13]. Therefore, novel formulation strategies, such as nanoparticles using cyclodextrin and lipid carriers to overcome its rapid degradation and enhance its solubility and bioavailability, are highly desirable [14-16].

In the last decade, crystal engineering has become an important formulation strategy in drug development because the newly discovered multicomponent crystal solid forms (i.e., cocrystals and salts) can fine-tune the active pharmaceutical ingredient (API)'s physiochemical properties (e.g., solubility, dissolution rate, physical and chemical stability, melting point, flowability, compressibility, hygroscopicity, and chemical stability, etc.), leading to improved bioavailability, efficacy and possibly reduced untoward effects [17-21]. Up to now, four multicomponent crystal forms of ATS have been reported, i.e., two salt forms of ATS with quinine (1:1) and cinchonidine (1:1) [22] and two cocrystal forms of ATS with 4,4'-bipyridine (2:1) [23] and nicotinamide (1:1) [24]. Based on the CSD (Cambridge Structural Database) search, the crystal structures of 2:1 ATS - 4,4'-bipyridine cocrystal (Refcode RUTJUO) and 1:1 ATS- cinchonidine salt (Refcode EZOSOE) have been successfully determined [22,23].

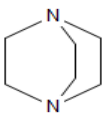
The aim of this work was to discover new multicomponent cocrystals/salts of ATS through extensive screening. In total, 117 potential coformer candidates were examined, including carboxylic acids, amino acids, nutraceuticals, and drug candidates for treating neglected tropical diseases (such as malaria and leishmania) (Table S1 in the supporting material). A mechanochemical solvent drop grinding (SDG) approach using methanol was used in the initial screening experiments. For those which were formed as gel-like resultants, further grinding was carried out with other solvents such as acetonitrile, ethanol, propan-2-ol, tetrahydrofuran, or acetonitrile. The samples were analysed by powder X-ray diffraction (PXRD), Fourier transform infrared spectroscopy (FTIR), and thermal analyses [i.e., differential scanning calorimeter (DSC), thermogravimetric analysis (TGA), and hot stage microscopy (HSM)] to confirm new crystal solid formation. As a result, five coformers shown in Figures 1(b)-(f) have been identified to form new multicomponent crystal forms with ATS, leading to five multicomponent forms. The determined stoichiometric composition and crystal structures were detected through the solution synthesis of single crystals suitable for X-ray structure determination. In the meantime, the ΔpK_a rule was used to identify the resultant multicomponent crystals as either cocrystals or salts [25-27]. Finally, the dissolution performance and stability of the new multicomponent solids in both aqueous solution and solid state at elevated stress conditions have been assessed.



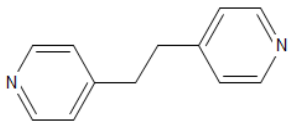
(a)



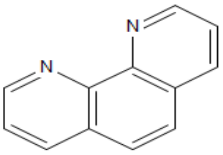
(b)



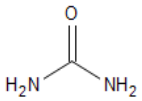
(c)



(d)



(e)



(f)

Figure 1: Chemical structures of the drug and cocrystal formers employed in the study: a) artesunate; b) 4-aminobenzoic acid; c) 1,4-diazabicyclo [2.2.2]octane; d) 1,2-di(pyridine-4-yl)ethane; e) 1,10-phenanthroline; f) urea

2. Materials and Methods

2.1 Materials

Artesunate (ATS, ≥97.5 % purity) was procured from Fisher Scientific (Loughborough, UK). Coformers listed in Table S1 in the supporting materials were obtained from numerous sources, including Fagron (Newcastle, UK), Cayman Chemicals (Michigan, USA), Alfa Aesar (Lancaster, UK), Sigma-Aldrich (Dorset, UK), and Arcos Organics (Geel, Belgium). HPLC grade of methanol (MeOH), propan-2-ol (IPA), ethanol (EtOH), acetonitrile (ACN), and analytical grade of acetone (ACE), diethyl ether (DEE), isobutanol (IBA), nitromethane (NMT), toluene (TOL), dichloromethane (DCM), ethyl acetate (EA), chloroform (CHFM) and extra dry grade of tetrahydrofuran (THF) employed in the experiments were purchased from Fisher Scientific (Loughborough, UK). Double Distilled Water (DDW) was internally produced using a Bi-Distiller (WSC044.MH3.7, Fistreem International Limited, Loughborough, UK) and was used throughout the study.

2.2 Method

2.2.1 ATS polymorph experimental screening

Solvent screening was carried out to discover the potential polymorphs of ATS. 100 mg of ATS was weighed and transferred into a 20 mL vial. An appropriate volume of each solvent was added, as indicated in Table S2 in the supporting materials. The mixture was then placed on a Multiposition Digital Hotplate Stirrer [Multi-HS Digital, 20865 Usmate (MB), Italy] operated according to the settings outlined in Table S2 for 10 min to ensure that all ATS crystals were dissolved completely. The samples were sealed with parafilm with small holes on the top, and they were then placed inside a fume cupboard to evaporate for 14 days at room temperature. The recrystallised products were characterised using PXRD, DSC, TGA, and FTIR.

2.2.2 Screening for cocrystals/salts via solvent drop grinding (SDG) method

Experimental screening tests using SDG were conducted to assess the coformers listed in Table S1. A weighed quantity of ATS and a coformer, totalling 200 mg at a 1:1 stoichiometric ratio, was placed in 15 mL stainless steel SmartSnap™ jars, each containing two 7 mm stainless steel grinding balls (Form-Tech Scientific, Montreal, Canada). Approximately 40 µL of MeOH was added to the mixture, and it was ground at room temperature in a Retsch mixer mill MM 400 (Retsch, Germany) for 30 min at a rate of 25 Hz. The ground samples were characterised by PXRD after stabilising for 30 min. Subsequently, further grinding and/or solvent evaporation were carried out with EtOH, ACN, IPA, THF, ACE, or DEE for the mixtures which formed gel-like products during the initial grinding experiments or where ATS transformed to DHA, and to investigate the potential existence of crystal solvates.

2.2.3 Preparation of powdered and single crystals by solvent evaporation (SE)

1) ***1:1 Artesunate - 4-Aminobenzoic Acid cocrystal (ATS-ABA):*** ATS-ABA powders were prepared using SE. a mixture of ATS (147.41 mg) and ABA (52.58 mg) was weighted into a 25 mL beaker with 1 mL of cosolvent (i.e., ACE and MeOH at a ratio of 70:30). The mixture was transferred unto a magnetic stirrer set at 50 ℃ and 200 rpm until the mixture was completely dissolved. The solution in the beaker was sealed using aluminium foil paper with holes created for evaporation. The single crystals of ATS-ABA were grown by dissolving 200 mg of the

cocrystal powders obtained above in 10 mL of DEE using a 25 mL beaker, which was sealed with parafilm, and a pinhole created to allow for slow evaporation. The single cocrystals were harvested in 5 days following complete evaporation of the solvent.

2) **2:1 Artesunate-1,4 - Diazabicyclo[2.2.2]octane cocrystal (ATS^2-DABCO) Form 1:** Powdered and single ATS^2-DABCO Form 1 were prepared using SE. ATS (87.26 mg) was weighed into a 25 mL beaker and dissolved in 15 mL DEE using a magnetic stirrer set at 30°C and 700 rpm. DABCO (12.73 mg) was also weighed into a 25 mL beaker and dissolved in 3 mL DEE on a magnetic stirrer set at 30°C and 200 rpm. The DABCO solution was then added into the ATS solution and mixed on a magnetic stirrer set at 30°C and 700 rpm. The resultant solution was sealed with foil paper with a pinhole created for slow evaporation. A mixture of powdered and single cocrystals was separated after evaporation within 5 to 6 days.

3) **2:1 Artesunate-1,4 - Diazabicyclo[2.2.2]octane salt (ATS²-DABCO) Form 2:** The same method as previously described above was employed, with the only difference being that this solid form can be synthesised from a mixture of ATS (77.51 mg) and DABCO (22.58 mg) at a 1:1 molar ratio, instead of ATS (82.26 mg) and DABCO (12.73 mg) at a 2:1 molar ratio.

4) ***2:1 Artesunate - 1,2-Di(pyridine-4-yl)ethane cocrystal (ATS^2-DPE):*** ATS^2-DPE powders were prepared using SE. ATS (67.60 mg) and DPE (32.39 mg) were weighed into a 25 mL beaker with 18 mL DEE. The mixture was transferred to a magnetic stirrer set at 30°C and 700 rpm until completely dissolved. The solution in the beaker was sealed with aluminium foil paper with a pinhole created for slow evaporation. The sample was left in a fume cupboard for 6 to 7 days for complete evaporation, resulting in pure powder at the bottom of the beaker, while single cocrystals adhered to the walls of the beaker.

5) ***1:1 Artesunate - 1,10-Phenathroline cocrystal (ATS-PHEN)****:* ATS-PHEN powders were prepared using SE. ATS (136.1 mg) and PHEN (63.8 mg) were weighed into a 25 mL beaker with 1 mL of THF. The mixture was transferred to a magnetic stirrer set at 50°C and 200 rpm until completely dissolved. The solution in the beaker was sealed with aluminium foil paper with holes created for evaporation. The sample was left in the fume cupboard for 24 h for complete evaporation to obtain the pure powders. The single cocrystals were grown by seeding with 10 mg of powder in the mixture solution, covered by the parafilm with a single pinhole for slow evaporation in the fume cupboard. The single cocrystals of ATS-PHEN were harvested between 24 to 48 hours by filtration.

6) ***1:1 Artesunate - Urea cocrystal (ATS-URE)*****:** ATS-URE cocrystal powders were prepared in IPA using SE. ATS (172.97 mg) and URE (27.02 mg) were weighed into a 25 mL beaker, and then 1 mL of IPA was added into the mixture, which was transferred to a magnetic stirrer set at 60°C and 230 rpm until it completely dissolved. The solution in the beaker was sealed with aluminium foil with holes created to allow the solvent to evaporation and then was left in the fume cupboard. The pure cocrystal powders were obtained after complete evaporation and confirmed by PXRD, FTIR, DSC, and TGA. To grow single cocrystals for structure determination, the mixture was dissolved in 2 mL of the cosolvent of IPA and HEX at a 60:40 ratio. The beaker was sealed with parafilm, and a pinhole was created to allow the solvent mixture for slow evaporation. The cocrystals were harvested after 5-6 days through filtration.

7) ***1:1:1 Artesunate - Urea Methanol cocrystal solvate (ATS-URE-CH_3OH):*** Single ATS-URE-CH_3OH cocrystals were grown using a cooling crystallisation method. ATS (172.97 mg) and URE (27.02 mg) were weighed into a 25 mL beaker with 2 mL of MeOH. The mixture was transferred to a magnetic stirrer set at 50°C and 200 rpm until completely dissolved. The solution in the beaker was sealed using parafilm with a pinhole. Single crystals of the ATS-Urea-CH_3OH were harvested by filtration after 6 to 8 h. The cocrystal powders were obtained by crushing the single cocrystals, which consistently formed large single crystals when dissolved in MeOH.

8) ***1:1:1 Artesunate - Urea Ethanol cocrystal solvate (ATS-URE-C_2H_6O):*** Powder and single cocrystals of ATS-URE-C_2H_6O were prepared using SE. ATS (172.97 mg) and URE (27.02 mg) were weighed into a 25 mL beaker with 2 mL of EtOH. The mixture was transferred to a magnetic stirrer set at 60°C and 230 rpm until completely dissolved. To obtain the cocrystal powders, the solution in the beaker was sealed using foil paper perforated with many small holes to facilitate fast evaporation. The cocrystal powders were obtained within four days. To obtain single cocrystals, the solution was seeded with 5 mg of cocrystal powders obtained above and sealed with parafilm with a pinhole created for slow evaporation. The single cocrystals of ATS-URE-C_2H_6O were harvested between 5 to 6 days through filtration. However, the structure of ATS-URE-C_2H_6O was not determined as the crystal was unstable.

9) ***1:1:1 Artesunate - Urea Acetonitrile cocrystal solvate (ATS-URE-C_2H_3N)****:* The powder and single cocrystals of ATS-URE-C_2H_3N were prepared using SE. ATS (172.97 mg) and URE (27.02 mg) were weighed into a 25 mL beaker with 2 mL of ACN. The mixture was transferred to a magnetic stirrer set at 60°C and 230 rpm until completely dissolved. To produce the cocrystal powders, the solution in the beaker was sealed using aluminium foil paper perforated with many small holes to facilitate fast evaporation overnight (24 h). To obtain the single cocrystals, 200 mg of ATS-URE-C_2H_3N solvate powder obtained from SE was dissolved in 1.5 mL ACN in a 25 mL beaker. The beaker was then sealed with parafilm with a pinhole created for slow evaporation. The sample was placed in a refrigerator, and the single cocrystals of ATS-URE-C_2H_3N were harvested within 1 to 3 h.

All powdered and single crystals produced were characterised using PXRD, DSC, HSM, TGA, FTIR, and single crystal X-ray diffraction (SXRD).

2.2.4 pKa value calculation

The p*Ka* values of ATS and the coformers (i.e., ABA, DABCO, DPE, PHEN and URE) were calculated using the ACD/ChemSketch version 2023.1.0 software by importing the structures from the built-in dictionary of the ACD/Percepta. The aqueous p*K*a values are calculated based on the Hammet-type equations for popular ionisable functional groups and carefully derived electronic substituent constants (σ) [28]. Other parameters considered for predicting p*Ka* using the classic algorithm include covalent hydration, Tautomeric equilibria, resonance effects, and α, β-unsaturated systems [29].

2.2.5 Degradation studies of ATS and its multicomponent crystals in solution

Solutions of ATS or its multicomponent crystal forms (except ATS[2]-DABCO Form 1) obtained with the equivalent ATS concentration of 100 µg/mL were prepared using either pure MeOH or a mixture of MeOH and DDW at different ratios (i.e., 50:50, 20:80, 10:90, and 5:95). The change of the ATS concentration in each of the prepared solutions was monitored using HPLC at regular intervals between 40 to 50 min over 24 h, with the temperature of the HPLC sampling tray not being controlled. The degradation rate of ATS in each solution was determined by the gradient of the plot of percentage concentration ATS remaining versus time.

2.2.6 Solid state stability studies of ATS and its multicomponent crystals under elevated conditions

A fixed amount of ATS or its cocrystal powders (except ATS[2]-DABCO Form 1) was packed in amber-coloured HPLC vials with a closed lid or uncapped and then placed in a stability chamber (HCP 105, Memmert, Germany) set at 50°C ± 1°C and a relative humidity (RH) of 75% ± 3%. Samples were evaluated at 0, 5, 10, 15, and 30 days using HPLC, PXRD, DSC, TGA, and FTIR to determine the percentages of the remaining ATS and solid form changes.

2.2.7 Solubility and dissolution studies of ATS and its multicomponent crystal powders

The apparent equilibrium solubility of ATS was measured in DDW. A mixture containing excess ATS in 20 mL of DDW was prepared in triplicate and transferred into a water bath set at 37 ± 0.5 °C with a rotation speed of 150 rotations per minute (rpm) for 24 h. Subsequently, the mixture was separated from the supernatant liquid by centrifugation for 2 min at 12,500 rpm using a Gusto Mini Centrifuge (Fisherbrand, China). The concentration of ATS in the supernatant liquid was determined using HPLC after dilution. Solid residues recovered after the solubility test were characterised using PXRD, DSC, TGA, and FTIR.

The dissolution profile of ATS or each of ATS multicomponent crystal powders with an equivalent amount of 150 mg ATS was employed under non-sink conditions using USP Apparatus 2 (DT 126, Erweka, Germany) at a speed of 50 rpm in 400 mL of DDW at 37 ± 0.5 °C. To reduce the effect of particle size on the dissolution rate, all materials were slightly ground by a mortar and pestle and sieved by a 60-mesh sieve (below 250 μm) prior to dissolution test. 1 mL of sample solution was withdrawn from the dissolution vessel at pre-set time points of 5, 10, 15, 30, 60, 120, 180 and 240 min. Supernatants were separated from the samples and analysed by HPLC to determine the concentrations of ATS. Solid residues recovered from each ATS dissolution test were air-dried at ambient temperature and analysed using PXRD, DSC, TGA, and FTIR. All experiments were repeated in triplicate.

The dissolution performance of ATS multicomponent crystals in comparison to raw ATS was assessed using the dissolution performance parameter (DPP) in Eq. (1) [30],

$$DPP = \frac{AUC_{multicomponent} - AUC_{ATS}}{AUC_{ATS}} \times 100 \quad (1)$$

where AUC is the area under the curve (AUC) of a dissolution profile, indicating the amount of drug dissolved throughout the dissolution time.

2.2.8 Crystal characterisations

1) Powder X-ray diffraction (PXRD) analysis: The PXRD patterns of solid powders were measured at ambient temperature using a Bruker D2 PHASER diffractometer equipped with a LYNXEYE XE-T detector (Bruker UK Limited in Coventry, UK). The X-ray source was Cu-Kα radiation operated at 30 KV and 10 mA to achieve the desired power. The sample was loaded onto the sample holder and analysed at a scanning rate of 0.02 ° per minute, within a 2–40° of 2θ range.

2) Measurement of Single crystal X-ray diffraction (SXRD)

   Single crystal diffraction data were collected using a Rigaku Synergy S diffractometer equipped with a dual beam (Cu, Mo) microfocus source and a Hypix 6000 detector. All data sets were collected using Cu Kα radiation at 100 K and processed with the CrysAlisPro package (Rigaku OD, *CrysAlisPro*, Rigaku Oxford Diffraction, Yarnton, England, 2023). The structures were solved and refined using the Olex2 [31] interface to SHELXT [32] and SHELXL [33], respectively. The positions of mobile acidic H atoms could be located from difference Fourier maps except for ATS^2-DABCO Form 2. In this structure, protonation states were assigned using C-O bond lengths in the carboxyl groups. For ATS-URE, we were unable to obtain a good quality single crystal. Each crystal tested showed significant diffuse scattering (Fig. S13 in the supporting materials) both at room temperature and at 100 K, which prevented the collection of a publishable quality data set. ATS-URE-C_2H_3N crystals showed elongated diffraction spots, indicating a strong tendency to form aggregates. The final data set was obtained by using a model of two twin components, The ATS-ABA structure revealed disorder of both ATS and ABA molecules. As there is considerable overlap between equivalent disordered atoms, distance similarity (SADI), rigid unit (RIGU) restraints and, in the case of ABA, equal displacement parameter (EADP) constraints were applied during refinement. A summary of data collection parameters is given in Table S3. The resulting structures were deposited with the CCDC (deposition numbers: CCDC 2427253 for ATS-ABA; CCDC 2427254 for ATS^2-DABCO Form 1; CCDC 2427255 for ATS^2-DABCO Form 2; CCDC 2427256 for ATS-PHEN; CCDC 2427257 for ATS-URE-CH_3OH; CCDC 2427258 for ATS-URE-C_2H_3N.

3) Differential Scanning Calorimetry (DSC) and Thermogravimetric (TGA) analyses: The thermal properties of solids were analysed using a NETZSCH DSC 214 Polyma instrument (NETZSCH instrument, Wolverhampton, UK) operated under a nitrogen atmosphere. The instrument was calibrated using indium metal. A sample of between 4 and 6 mg was analysed in an aluminium pan with a pierced pinhole lid. Measurements were conducted at a heating rate of 20 °C/min with a temperature range of 20 to 300 °C. The decomposition and presence of solvent of solid samples were measured by a NETZSCH TG 209 F3 Tarsus (NETZSCH instrument, Wolverhampton, UK) operated under a nitrogen atmosphere. A sample was analysed in a ceramic pan with no lid. Measurements were carried out with a heating rate of 20 °C/min with a temperature range from 30 to 700 °C.

4) Fourier Transform Infrared Spectroscopy (FTIR): The FTIR spectra of the solid samples were collected using an ALPHA interferometer (Bruker UK Limited, Coventry, UK) equipped with a horizontal universal attenuated total reflectance (ATR) accessory. For each sample (4-8 mg), an average of 30 scans was collected per spectrum with a resolution of 2 cm^{-1} in the spectral region of 400 to 4000 cm^{-1} using the OPUS software at room temperature.

5) High-Performance Liquid Chromatography (HPLC): The concentrations of ATS and DHA in the solution were determined using an Agilent Series 1100 automatic HPLC system equipped with a diode array detector and a Roc C18 column (5 µm, 150x4.6 mm, Restek Thames, High Wycombe, UK) at 25 °C. An isocratic method was utilised with a mobile phase consisting of 60 % acetonitrile and 40 % mixture of DDW and MeOH (at a ratio of 3:2) at a flow rate of 0.6 mL/min. ATS and DHA concentrations were detected at a wavelength of 210 nm. ATS and DHA calibration samples were prepared in MeOH within a concentration range of 5 to 500 µg/mL and 1.875 to 150 µg/mL, respectively. The calibration models can be found in Tables S7&8 in the supporting materials.

6) Polarised Light microscopy: The morphology of single crystals was observed using a LEICA DM750 polarised light microscope (Leica Microsystems Ltd., Milton Keynes, U.K.) equipped with a 10x magnification video camera. The operating software used was Studio Capture (v4.0.1, Roland, Reading, UK).

7) Particle size distribution analysis: To determine the particle size distribution of solid powders, a Microtrac Sync analyser (utilising the Turbo Sync module) was used, with configurations of a dispersion pressure of 0.5 psi, a runtime of 40 seconds and an absorbing transparency feature with an irregular shape algorithm. The dry powder samples, approximately 100 mg to 200 mg depending on powder density, were evenly distributed on the sample tray and introduced into the measurement system. The results of the particle size, distribution, and morphology were determined using combined laser diffraction with dynamic image analysis by the Microtrac Flex software (v12.0.1.1).

8) Hot stage microscopy (HSM): The melting thermograms of ATS-ABA, ATS^2-DABCO Form 1, and ATS^2-DABCO Form 2 were also determined using the hot stage (FP82HT Mettler Toledo with FP90 control processor, Ohio, United States) connected to a Leica DM750 polarised light microscope. The multicomponent cocrystal powders, weighing about 1 to 2 mg, were evenly spread onto a cavity slide covering the pinhole of the hot stage and covered with a glass cover slip. The machine operated at 20 °C/min from 40 to 200 °C. Studio Capture (v4.0.1, Roland, Reading, UK) captured the melting process.

2.2.9 Predictions of the PXRD patterns and morphologies of ATS multicomponent crystals

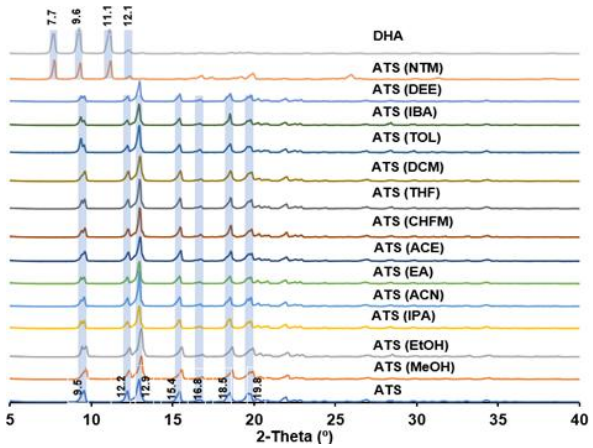
The PXRD patterns of the ATS multicomponent crystals were predicted based on the crystal structures determined by SXRD using the powder pattern tool in CCDC Mercury (v2023.3.0). The prediction covered a range between 2 to 40° of 2θ, with a scanning step size of 0.02°, using a wavelength set at 1.54056 Å. The pattern was configured to include hydrogen in the analysis. Additionally, the morphology of single crystals was predicted using the Bravais, Friedel, Donnay and Harker **(**BFDH) model available in the CSD-Particle menu of the same software.

3 Results and Discussion

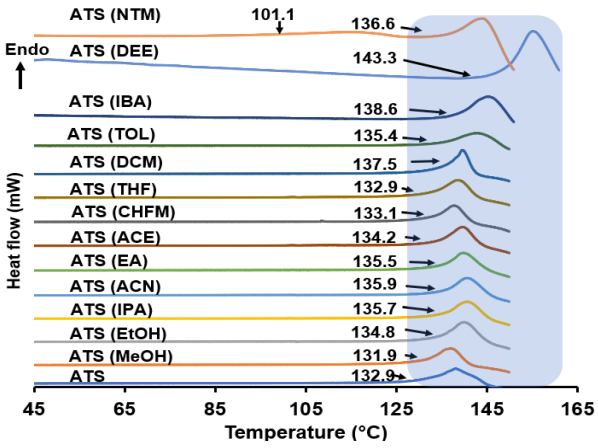
3.1 ATS polymorph screening and assessment

The solvent screening results indicated that ATS was soluble in 13 organic solvents used (i.e., MeOH, EtOH, IPA, ACN, EA, ACE, CHFM, THF, DCM, TOL, IBA, DEE, and NTM shown in Table S2) whilst it was practically insoluble in n-Hexane and n-Heptane. There is no new crystalline form of ATS observed, showing that the PXRD patterns of the recrystallised solids from those soluble solvents except NTM are in good agreement with the initial ATS samples, showing the characteristic peaks at 9.5°, 12.2°, 12.9°, 15.4°, 16.8°, 18.5°, and 19.8° in Figure 2(a) [22]. In the case of the solids recrystallised from NTM, apart from the ATS characteristic peaks at 16.8° and 19.8°, distinctive peaks were observed at 7.7°, 9.6°, 11.1°, and 12.1° of 2θ, corresponding to the DHA characteristic peaks [34]. This suggests that some ATS has been transferred into DHA in NTM, and then a mixture of ATS and DHA crystals has been recrystallised during SE.

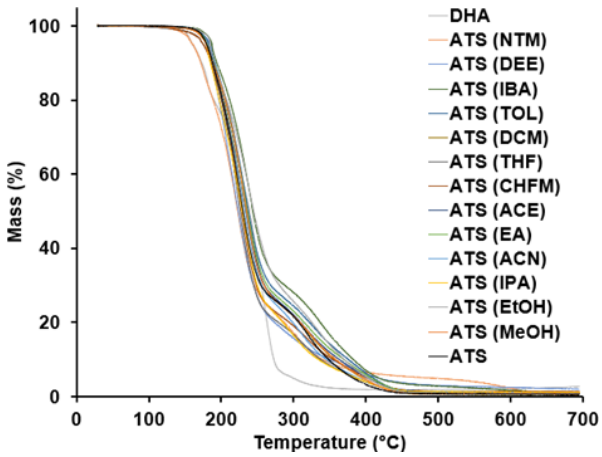
The similar thermal behaviours of the raw ATS and recrystallised ATS samples are also obtained, as shown in DSC and TGA analysis [Figures 2(a)&(b)]. DSC results [Figure 2(b)] reveal that the melting point of raw ATS was 132.9 °C while the melting points of the recrystallised samples were at the range from 131.9 °C to 143.3 °C, which is within the melting point range for artesunate reported in the literature [22,35]. In the TGA profiles, the onset of the ATS decomposition was 151.8 °C for the raw ATS and 106.5 °C to 152.3 °C for the recrystallised solids [Figure 2(c)], which is in good agreement with the literature data [36]. As the recrystallised solids from NTM are a mixture of ATS and DHA, the DSC and TGA profiles differ from those of either ATS or DHA, shown in Figure S1 in the supporting materials. The same observations are also obtained based on the FTIR results shown in Figure S2.



(a)



(b)



(c)

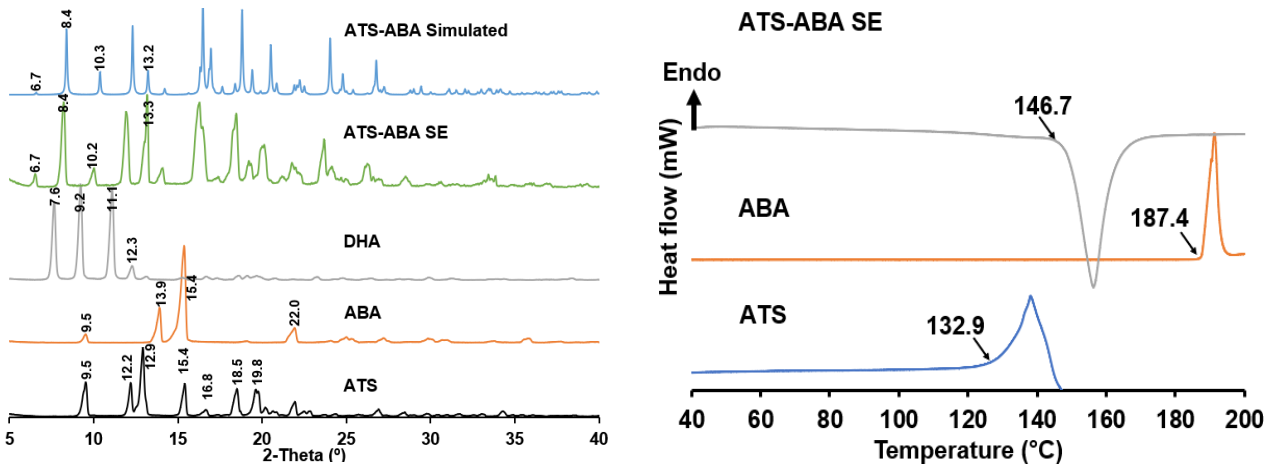
Figure 2: Comparison of raw and recrystallised ATS: (a) PXRD results; (b) DSC results; (c) TGA results.

3.2 Cocrystal/salt screening and characterisation

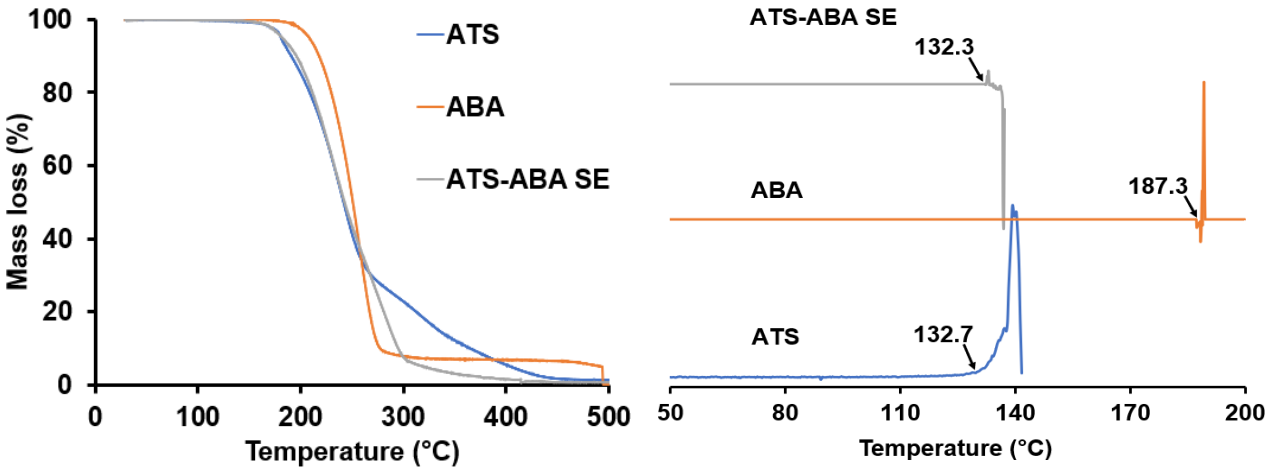
Experimental screening between ATS and each of the 117 coformers in Table S1 was performed in a 1:1 stoichiometric ratio using SDG and/or SE methods. Initially, MeOH was selected as the grinding solvent based on a previous report in the literature [22]. Subsequently, additional solvents (EtOH, ACN, IPA, THF, or ACE) were employed for the compounds that formed as gel-like products or transformed to DHA and to screen for potential ATS-URE cocrystal solvates. Furthermore, SE using DEE was carried out for 20 coformers (PG, RSV, DPE, PIR, APR, SAC, HU, PZQ, NIC, DHBA, TFA, INH, PZA, IMZ, PHZ, PIZ, NA, MEA, L-PRO and DABCO) based on similar structures that formed multicomponent crystals with ATS as reported in the literature [23].

The resultant samples were evaluated using PXRD, summarised in Table S4 in the supporting materials. If loss of the characteristic diffraction peaks from the starting raw materials and/or formation of new diffraction peaks were observed, it indicated the potential formation of a new crystalline form. It was found that seven coformers, including 5FC, FLZ, FFA, GCV, QUE, MBZ, and ASP-TM, underwent a phase transformation in the physical mixture with ATS when ground with MeOH. In contrast, ATS was converted to DHA in the mixture with GLA, OA, PIZ, APR, DHBA, or IMZ in the screening experiments using either grinding or SE with MeOH. In summary, the potential coformers for the formation of multicomponent crystal forms with ATS were ABA, DABCO, DPE, PHEN, and URE.

A mixture of ATS and ABA, when ground with MeOH or ACE in a 1:1 stoichiometric ratio, showed a physical mixture or partial transformation (Table S4). Further grinding with ACE resulted in partial cocrystal formation without losing the ATS characteristic peaks. However, when a cosolvent of MeOH and ACE was used for SE of the mixture, formation of a pure cocrystal was observed, as shown in Figure 3(a), in which the ATS characteristic peak at 9.5° (110) was lost and new peaks were observed at 6.7° (001), 8.4° (011), 10.2° (020), and 13.3° (002) of 2θ. The DSC thermogram [Figure 3(b)] of the solids demonstrated a broad exothermic peak with an onset temperature of 117.3°C. This peak could be attributed to the decomposition of the solid samples. In contrast, the HSM thermogram [Figure 3(d)] shows that the onset of melting point for ATS-ABA cocrystal is 132.3°C, which is lower than that of the starting materials. The TGA thermogram [Figure 3(c)] shows the weight loss temperature was 151.8°C, which was higher than the melting point determined by HSM, thus supporting the DSC results.



(a) (b)

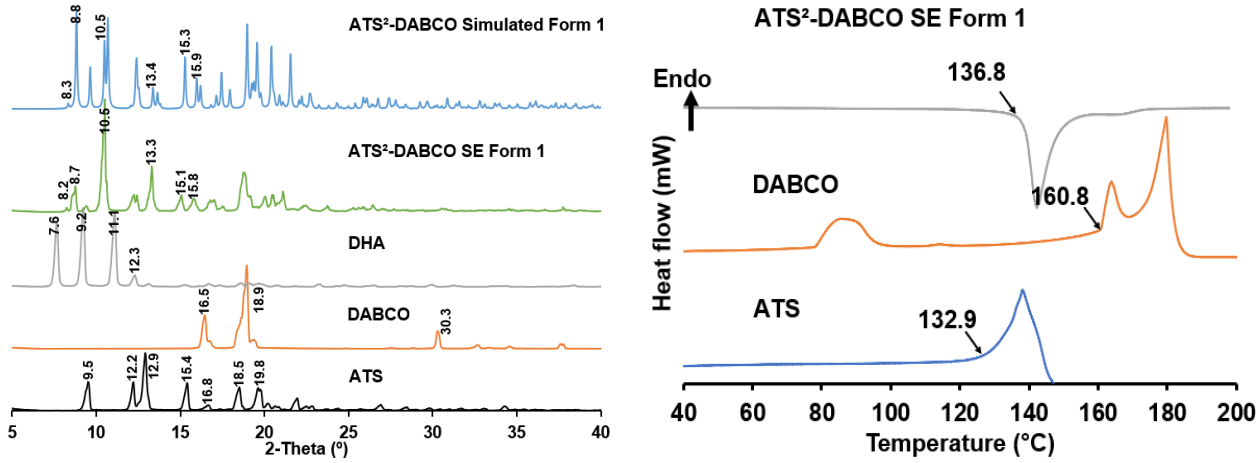


(c) (d)

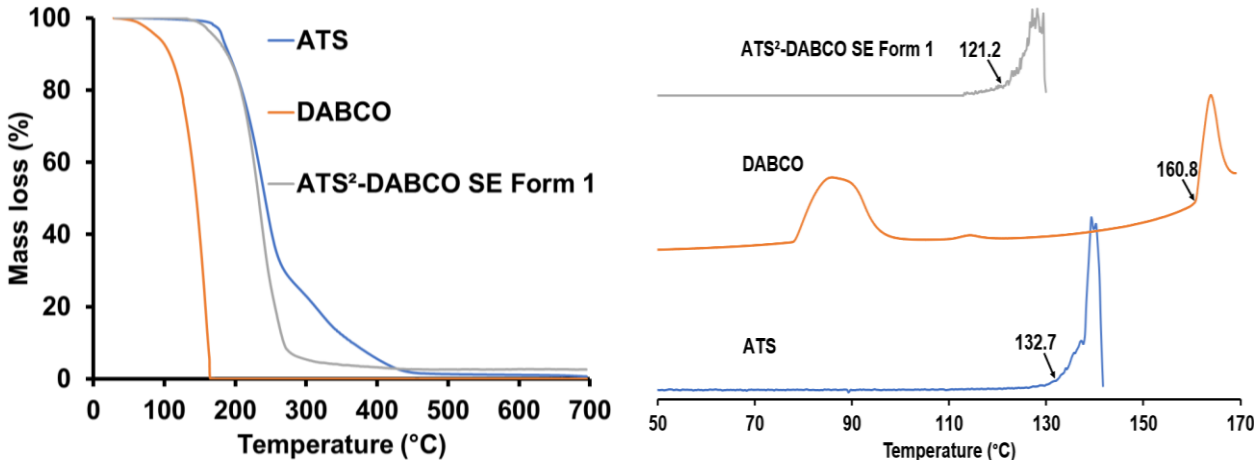
Figure 3: Characterisation of ATS-ABA cocrystal of a) PXRD; b) DSC; c) TGA and d) HSM results

DABCO was initially screened by SE with MeOH at a 1:1 stoichiometric ratio, resulting in the transformation of ATS to DHA, as shown in Table S4 of the supporting materials. Further screening was later carried out by SE using DEE for the stoichiometric ratios of 1:1 and 2:1, leading to the formation of two separate 2:1 ATS-DABCO crystals. While the 2:1 ATS-DABCO Form 1 (Figure 4) can only be formed from a 2:1 mixture of ATS and DABCO in DEE, the 2:1 ATS-DABCO Form 2 (Figure 5) can be formulated from both a 1:1 mixture, and occasionally, from a 2:1 mixture of ATS and DABCO in DEE.

The ATS[2]-DABCO form 1 is shown in the PXRD patterns in Figure 4(a); the ATS peaks were lost at 12.9° (201), 15.4° (211) and 18.5° (102) and new peaks were present at 8.2° (002), 8.7° (10-1), 10.5° (101), 13.3° (102), 15.1° (013) and 15.8° (112) of 2θ. The DSC thermogram shown in Figure 4(b) indicates a broad exothermic peak with an onset at 136.8 °C, attributed to the decomposition of the solids. Melting at 121.2° C was confirmed using the HSM thermogram, shown in Figure 4(d), and the TGA results shown in Figure 4(c) demonstrated no weight loss below 100 °C.



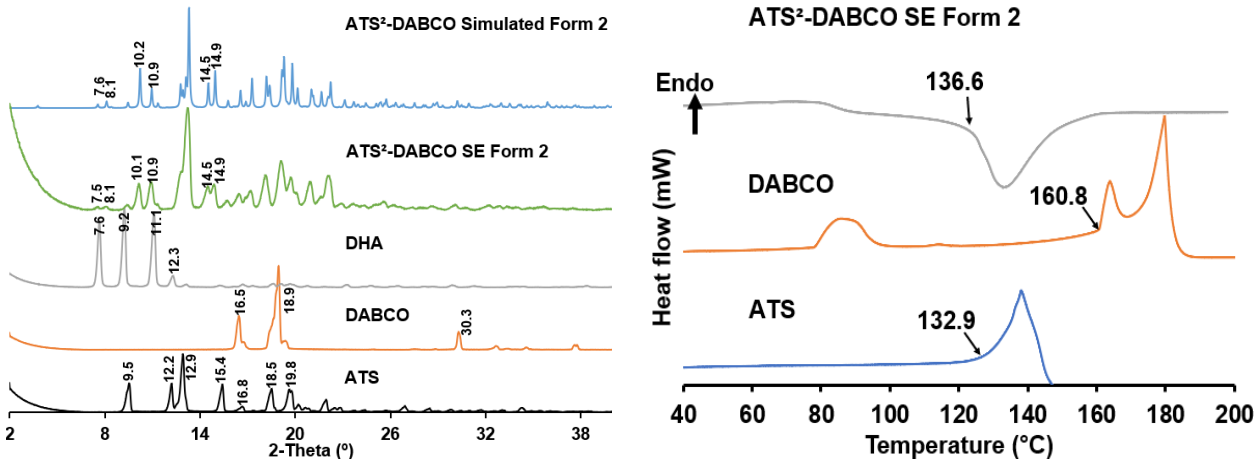
(a) (b)



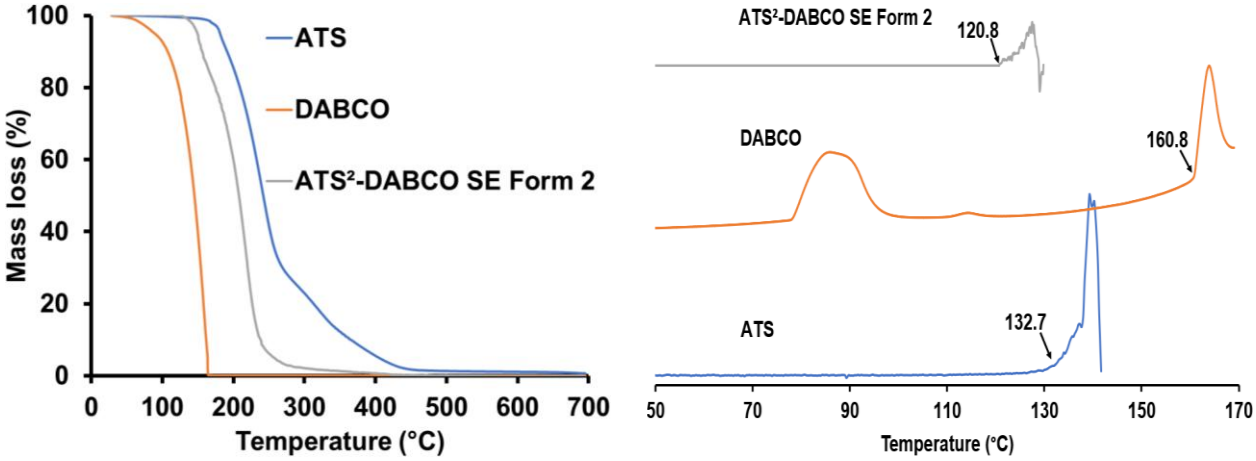
(c) (d)

Figure 4: Characterisation of ATS[2]-DABCO Form 1 of a) PXRD; b) DSC; c) TGA; d) HSM results

The PXRD pattern of ATS[2]-DABCO Form 2 [Figure 5(a)] is characterised by the loss of ATS peaks at 12.2° (011) and 15.4° (211), along with the appearance of new peaks at 7.5° (002), 8.1° (100), 10.1° (10-2), 10.9° (011), 14.5° (11-2), and 14.9° (103) of 2θ. In the DSC analysis [Figure 5(b)], a broad exothermic peak was observed, which could be attributed to decomposition, as confirmed by the TGA thermogram [Figure 5(c)] showing a lower decomposition temperature of 133.1 °C compared to ATS. Furthermore, HSM analysis [Figure 5(d)] confirmed a melting endotherm at 120.8°C.



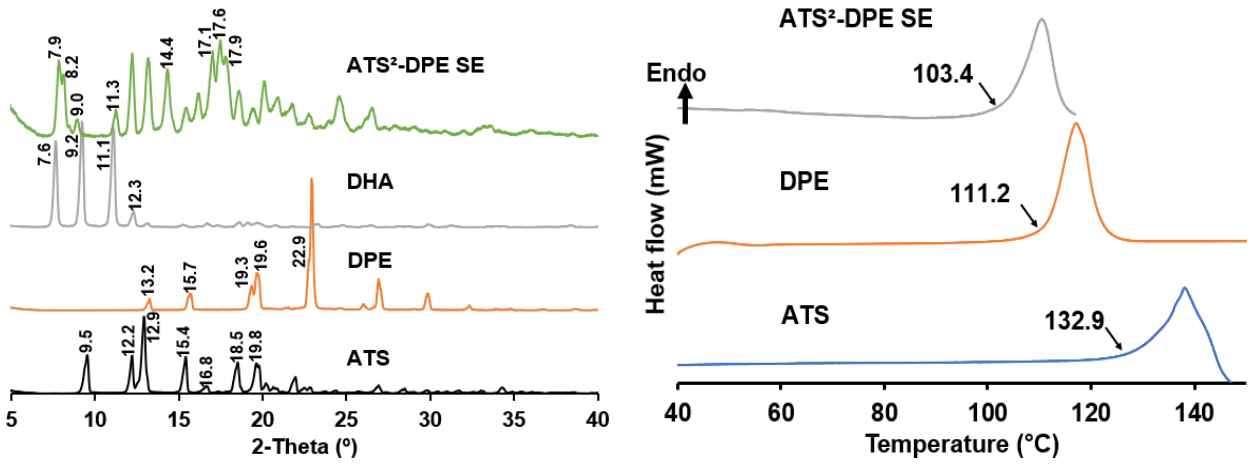
(a) (b)



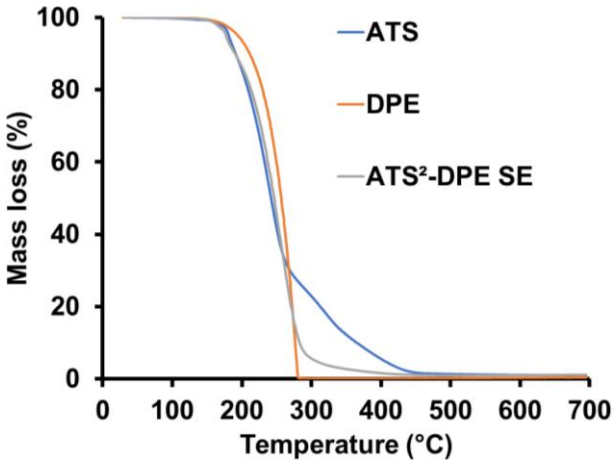
(c) (d)

Figure 5: Characterisation of ATS[2]-DABCO Form 2 of a) PXRD; b) DSC; c) TGA; d) HSM results

The screening of ATS with DPE was initially conducted using SDG and neat grinding, resulting in sticky gel products which cannot be characterised by PXRD. Subsequently, SE with MeOH was performed, resulting in the transformation of ATS to DHA, as indicated in Table S4 of the supporting materials. Further, SE experiments were carried out using DEE reported in the literature [23], leading to the formation of 2:1 ATS-DPE cocrystal evidenced by loss of the ATS peak at 9.5° and the appearance of new peaks at 7.9°, 8.2°, 9.0°, 11.3°, 14.4°, 17.1°, 17.6°, and 17.9° of 2θ. As SXRD had already determined a similar structure for ATS[2]-BPY previously [23], ATS[2]-DPE SE was evaluated using solvent evaporation with DEE [Figure 6(a)], yielding the same PXRD pattern observed with a 1:1 stoichiometric ratio. Therefore, both 1:1 and 2:1 ratios of ATS-DPE produced the same form, as confirmed by the PXRD pattern. The DSC thermogram [Figure 6(b)] exhibited a melting endotherm at 103.4°C, lower than the melting endotherms of both starting materials. TGA results [Figure 6(c)] support the findings from DSC, with no mass loss observed at temperatures up to 154°C.



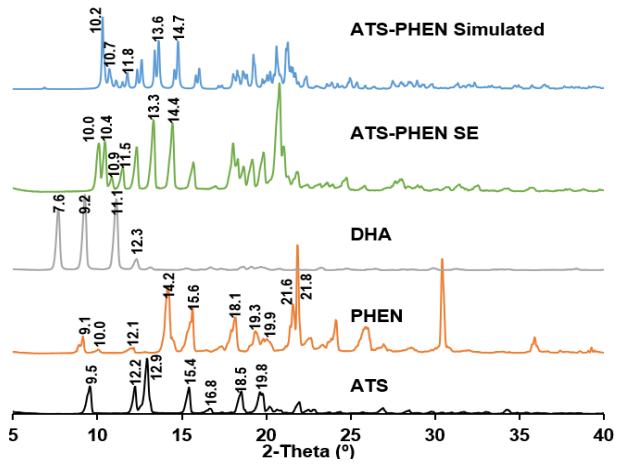
(a) (b)



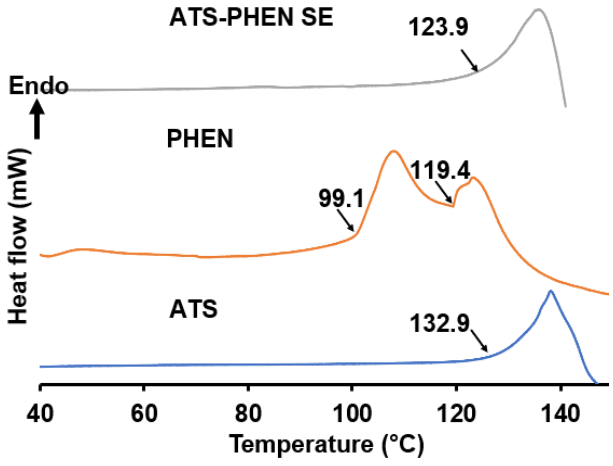
(c)

Figure 6: Characterisation of ATS[2]-DPE cocrystal of a) PXRD; b) DSC and c) TGA results

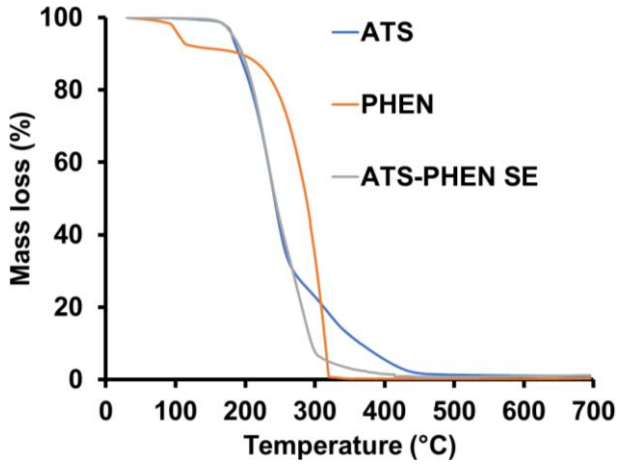
In the initial screening of ATS and PHEN with MeOH (Table S4 in the supporting materials), the PXRD patterns revealed the formation of a physical mixture, as none of the characteristic peaks of the original starting materials were lost and no new peak was observed. Because PHEN has a similar structure to BPY, which has been reported to form ATS[2]-BPY cocrystal [23], further screening was conducted using THF, resulting in a new cocrystal from both SDG and SE, as indicated in Table S4 and Figure 7(a). This was accompanied by the loss of characteristic ATS peaks at 9.5° (110), 12.9° (201), 15.4° (211), and 16.8° (020) of 2θ, while new peaks appeared at 10.0° (060), 10.4° (11-1), 10.9° (021), 11.5° (031), 13.3° (051), and 14.4° (061) of 2θ. The melting endotherm at 123.9°C for the 1:1 ATS-PHEN cocrystal, as depicted in Figure 7(b), falls between the melting endotherms of the two original starting materials, ATS (132.9°C) and PHEN (119.4°C). The TGA thermogram of the ATS-PHEN cocrystal showed no significant weight loss below the melting endotherm, confirming no solvate formation.



(a)



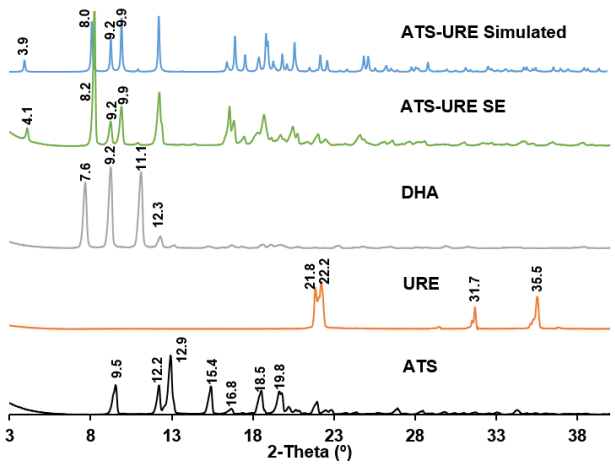
(b)



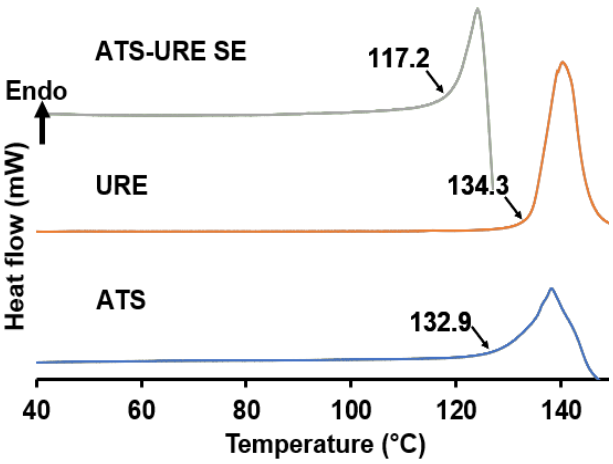
(c)

Figure 7: Characterisation of ATS-PHEN cocrystal of a) PXRD; b) DSC; c) TGA results

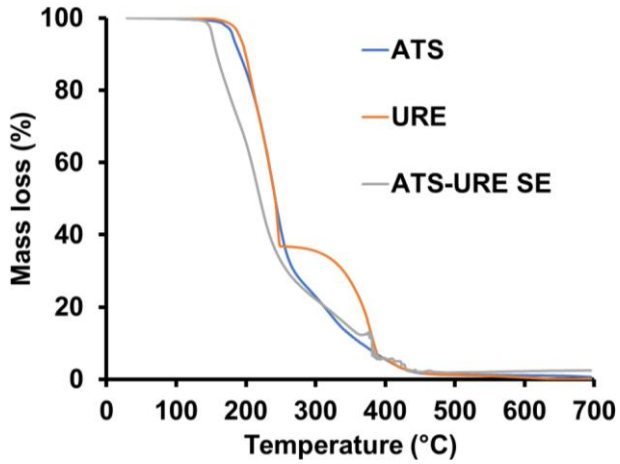
Initial grinding of the mixture of ATS-URE with IPA resulted in partial formation (Figure S4 in the supporting materials). Pure ATS-URE powders were generated by SE in IPA, with new peaks formed at 4.1° (002), 8.2° (004), 9.2° (011), and 9.9° (012) of 2θ and loss of two of the major ATS peaks at 9.5° (011) and 12.9° (102) of 2θ in Figure 8(a). Thermograms from DSC [Figure 8(b)] demonstrate the formation of a new crystalline solid (ATS-URE cocrystal) with a lower endothermic melting peak at 117.2°C when compared to the original starting materials of ATS at 132.9°C and URE at 134.3°C. The TGA results of the ATS-URE cocrystal [Figure 8(c)] validated the DSC results for forming a pure cocrystal, showing a different onset temperature of the weight loss profile from those of ATS and URE. Additionally, the absence of weight loss of the cocrystal powders at a temperature of up to 100°C indicates the absence of volatile components or solvents being removed.



(a)



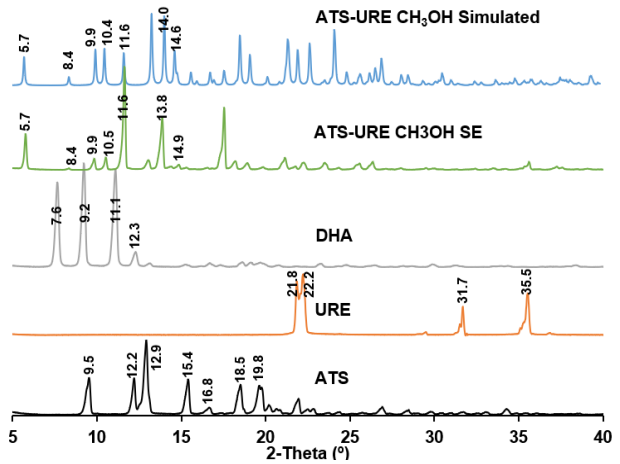
(b)



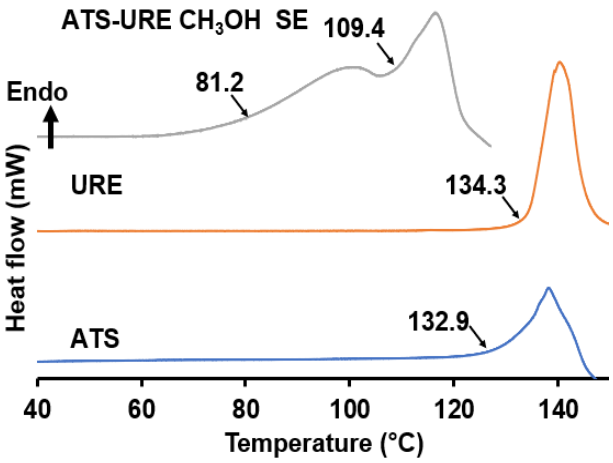
(c)

Figure 8: Characterisation of ATS-URE cocrystal of a) PXRD; b) DSC; c) TGA results

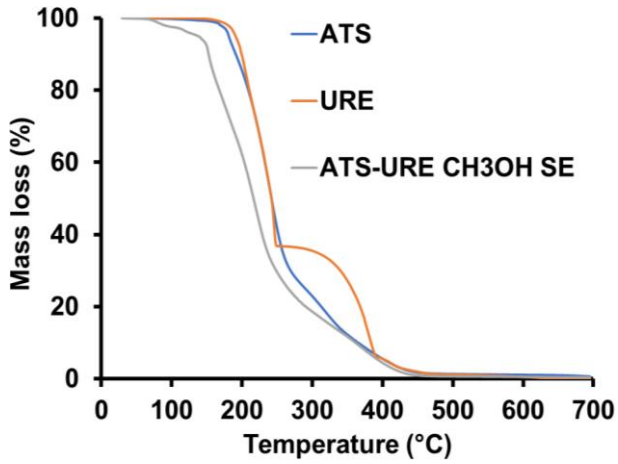
The SDG of the mixture of ATS and URE with MeOH resulted in a potentially different crystal form, as shown in the supporting materials' PXRD patterns in Table S4. Similar diffractograms were observed following a SE experiment in MeOH in Figure 9(a), with ATS characteristic peaks missing at 9.5° (110) and 12.2° (011) of 2θ and new peaks noticed at 5.7° (001), 8.4° (100), 9.9° (10-1), 10.5° (101), 11.6° (002), 13.8° (10-2), and 14.9° (102) of 2θ. Characterisation using DSC in Figure 9(b) demonstrated the formation of a new multicomponent cocrystal with an endothermic melting peak at 109.4 °C, lower than the original starting materials. However, a broad and indistinct endothermic event was observed before the melting endotherm at 81.2 °C, suggesting the formation of a multicomponent cocrystal solvent. SXRD subsequently confirmed this in Figure 17, which identified it as ATS-URE-CH_3OH. The TGA result in Figure 9(c) supports the DSC findings, indicating the formation of a cocrystal solvate with a 7.2 % weight loss occurring around 77 °C, which can be attributed to the loss of MeOH as theoretical loss MeOH content in the ATS-URE-CH_3OH cocrystal is 6.7 %.



(a)



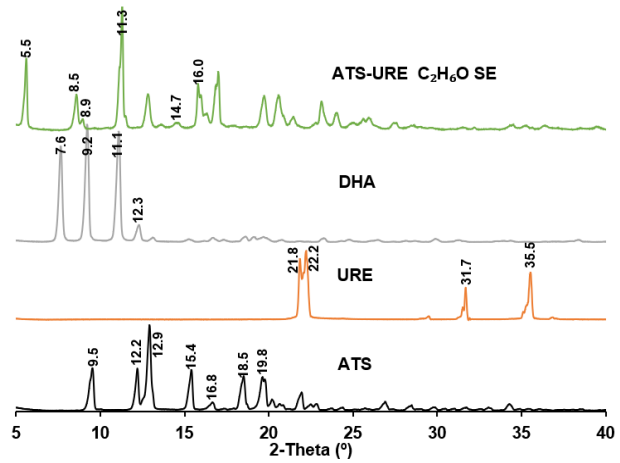
(b)



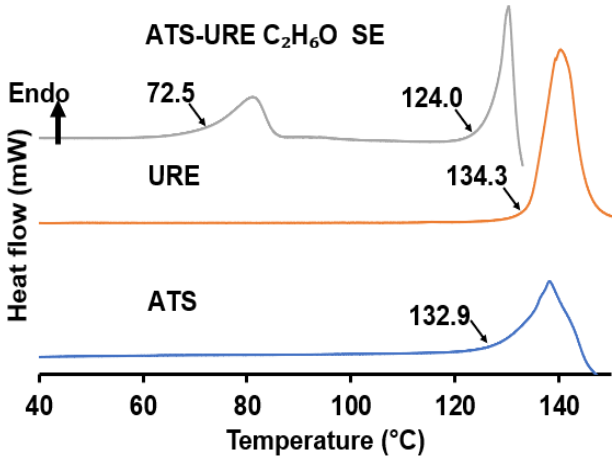
(c)

Figure 9: Characterisation of ATS-URE-CH_3OH cocrystal solvent of a) PXRD; b) DSC; c) TGA results

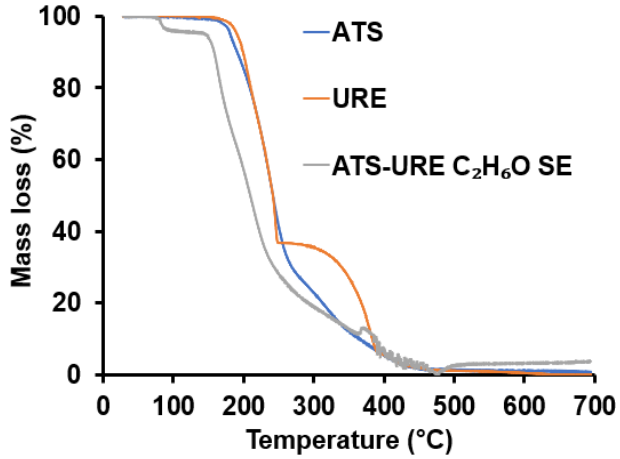
The PXRD results of the ground mixture of ATS and URE with EtOH (Table S4 in the supporting materials) showed a partial transformation indicated by the appearance of new peaks at 5.5, 8.5, 8.9, 11.3, 14.7, and 16.0° of 2θ°. However, the characteristic peaks of ATS were all kept in the PXRD result. The PXRD pattern of the solids obtained by SE in EtOH, as depicted in Figure 10(a), indicate the loss of a significant characteristic peak of ATS at 12.2° (011) of 2θ, suggesting the formation of a new cocrystal. The thermograms obtained from DSC in Figure 10(b) indicated a melting endotherm for the new cocrystal at 124 °C. An initial endotherm was also observed at 72.5°C, which could be attributed to the loss of EtOH. The Thermogravimetric Analysis (TGA) thermogram in Figure 10(c) corroborated the DSC results, showing a sharp 6 % weight loss at 78°C, which could be associated with removing EtOH. Although single crystals of ATS-URE-C_2H_6O have been successfully grown from EtOH (Table S7 in the supporting materials), they were unstable, making it impossible to determine its crystal structure using SXRD.



(a)



(b)



(c)

Figure 10: Characterisation of ATS-URE-C_2H_6O cocrystal solvent of a) PXRD; b) DSC; c) TGA results

When a mixture of ATS and URE with ACN was ground, the PXRD results (Table S4) revealed the formation of a new crystal form. Characteristic peaks of ATS were no longer visible at 9.5° (110), 12.2° (011), and 12.9° (201) of 2θ while new peaks emerged at 5.8° (001), 8.3° (100), 9.7° (10-1), 10.6° (101), 11.7° (002), 12.6° (011), 13.9° (110), and 14.8° (110) of 2θ. Similar PXRD patterns were obtained for the solids generated from SE and SDG in ACN, shown in Figure 11(a) and Table S4 of the supporting document. However, it has to stress that there are discrepancies between the simulated and measured XRD patterns. The issue is most likely related to the impurity of DHA in the cocrystal samples collected. We have tried to produce the pure ATS-URE-C_2H_6O cocrystal powders, but a small amount of the DHA always exists due the stability issue of ATS. In the DSC analysis [Figure 11(b)], an endothermic melting peak for the novel cocrystal was noted at 86.6°C. This was preceded by a broad endothermic peak at 59.2°C, suggesting solvent loss and indicating the formation of a cocrystal solvate. Confirmation of this was provided by SXRD, revealing the composition as 1:1:1 ATS-URE-C_2H_3N, as shown in Figure 18. The TGA thermogram [Figure 11(c)] further substantiated the DSC results, displaying a sharp mass (8.6 %) loss at around 78.6°C.

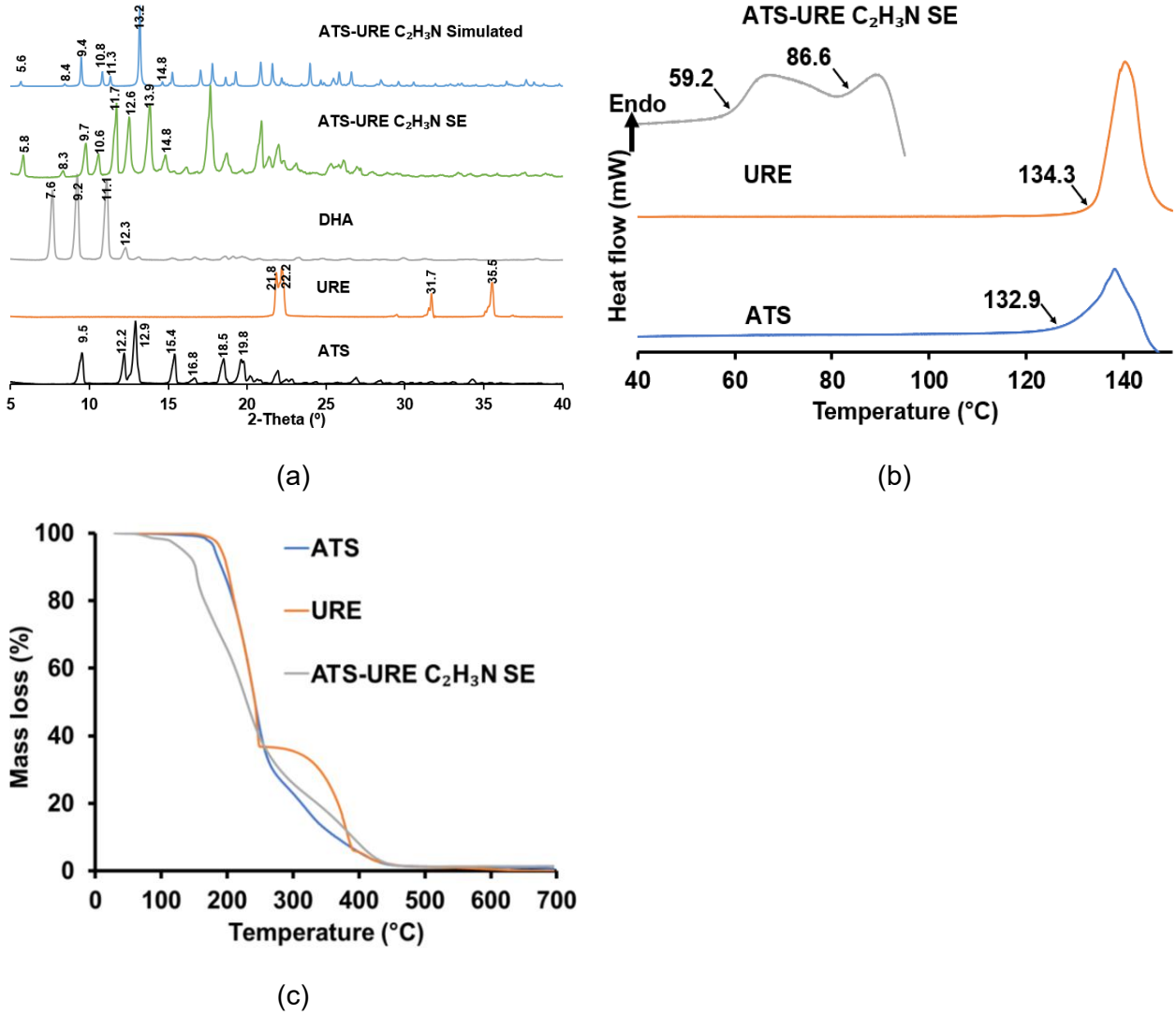


Figure 11: Characterisation of ATS-URE C_2H_3N cocrystal solvent of a) PXRD; b) DSC; c) TGA results

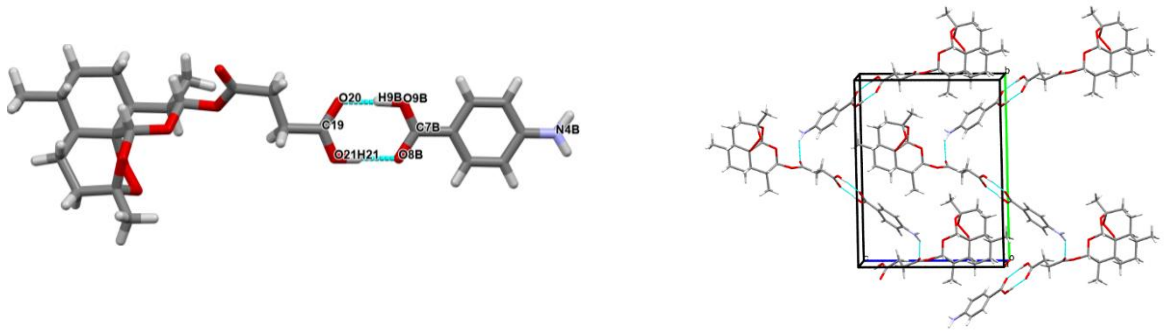
The FTIR spectra of ATS and novel ATS multicomponent solids are presented in Table S6 in the Supporting Materials. Based on these FTIR spectra of the ATS multicomponent crystals, all of them are cocrystals except that ATS[2]-DABCO Form 2 could be a salt form. Details of the analyses could be found in Table S6 in the Supporting Materials. Additionally, changes in peak intensities or broadening of peaks may signify alterations in crystal packing and the multicomponent structural arrangement.

3.3 ATS cocrystals structure analyses

Fairly good single ATS cocrystals for SXRD measurements were grown using the slow SE method, as detailed in Sections 2.2.3 and 2.2.8.

ATS-ABA cocrystal: The ATS-ABA cocrystal structure, resolved by SXRD, demonstrates the formation of a supramolecular homosynthon in the monoclinic system with a space group of $P2_1$, stabilised by hydrogen bonding between the two carboxylic acid groups of ATS and ABA [Figure 12(a)]. The observed disorder (Table S5) suggests libration of the whole dimer along the axis connecting the two carbonyl C atoms. The measured CO bond lengths of ATS shown in Table 1 reveal a slight elongation of the C19-O21 bond, which is a typical characteristic of carboxylic acid dimers. An extension of the dimers through hydrogen bonds of N-H…O(ester) between ABA and ATS leads to the formation of corrugated chains, which assemble to form a sheet structure, shown

in Figure 12(b). The sheets then stack to give the final 3-D structure with the support of N-H…O(ether) hydrogen bonds.



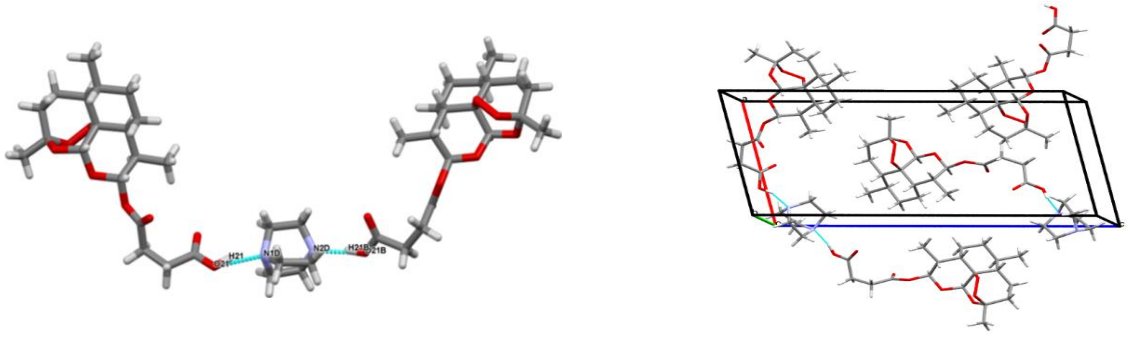
(a) (b)

Figure 12: Crystal structure packing of ATS-ABA cocrystal: a) Supramolecular synthon linked dimer ATS-ABA; b) Crystal packing structure. Only one disorder component is shown for clarity.

Table 1: C=O and C-O Bond Distances of the Carboxylic Acid Group in ATS Cocrystals

ATS cocrystals	C19-O20 (Å)	C19-O21 (Å)	Note
ATS-ABA	1.246(3)	1.278(3)	Carboxylic acid dimer
ATS^2-DABCO Form 1	1.212(4) 1.209(4)	1.306(3) 1.317(3)	-
ATS^2-DABCO Form 2	1.208(11) 1.255(12)	1.353(9) 1.299(10)	+NH...O-
ATS-PHEN	1.189(7) 1.214(4) 1.209(4)	1.320(7) 1.322(4) 1.322(4)	-
ATS-URE-CH_3OH	1.206(4)	1.322(4)	-
ATS-URE-C_2H_3N	1.212(7)	1.314(7)	-

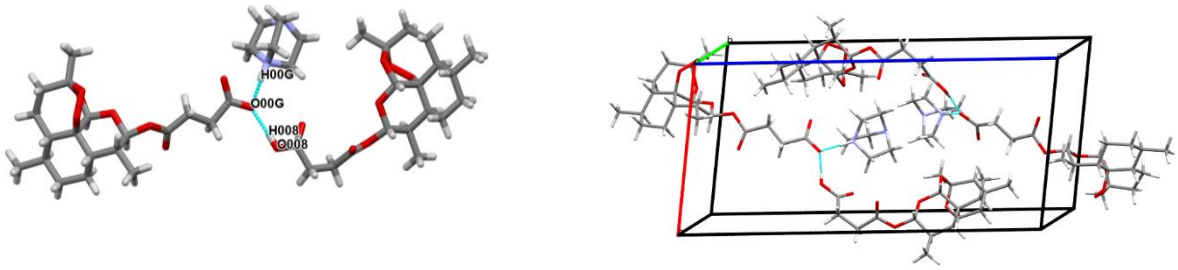
ATS^2-DABCO cocrystal Form 1: The crystallographic analysis of ATS^2-DABCO Form 1 reveals a monoclinic crystal system with space group $P2_1$, featuring a hydrogen-bonded trimer among two ATS and one DABCO. The components of the cocrystal are linked through O-H…N hydrogen bonds in the trimer structure shown in Figure 13(a). The trimer units form the overall packing through van der Waals interactions, to give the final 3-D structure in Figure 13(b). The C-O bond length data in Table 1, combined with the lack of significant elongation or shortening characteristics of proton transfer, confirms ATS^2-DABCO Form 1 as a cocrystal.



(a) (b)

Figure 13: Crystal structure packing of ATS^2-DABCO form 1 cocrystal: a) Supramolecular synthon linked dimer ATS^2-DABCO; b) Crystal packing structure

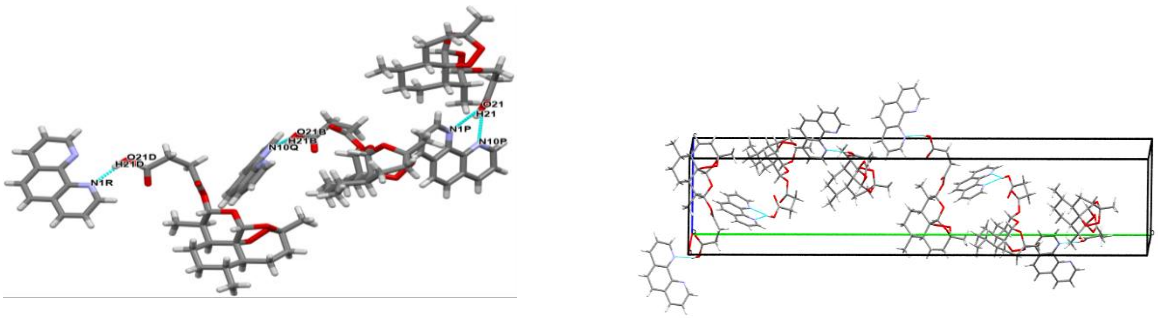
ATS^2-DABCO salt Form 2: The carboxyl C=O bond lengths for one of the ATS molecules clearly indicate that it is a carboxylic acid in Table 1. In the other ATS molecule, these bond lengths have intermediate values between single and double bonds, suggesting at least partial proton transfer. To reflect this the proton was placed on the DABCO N atom. The supramolecular synthon in the trimer of ATS^2-DABCO Form 2 is shown in Figure 14(a), in which a hydrogen bond of O-H…O(-) of the two ATS is formed and it is also linked to (+)N-H of DABCO. Similar to Form 1, the DABCO molecules form weak interaction with the ATS in the other trimer, which stack on each other to give a final 3-D structure in Figure 14(b).
The final difference Fourier map of this crystal structure (Figure S14) indicates the possibility that partial degradation of ATS may have occurred during crystallisation. Unfortunately, the small difference peaks did not allow for unambiguous identification of this minor component.



(a) (b)

Figure 14: Crystal structure packing of ATS^2-DABCO salt form 2: a) Supramolecular synthon linked dimer ATS^2-DABCO; b) Crystal packing structure

ATS-PHEN cocrystal: The crystallographic analysis of ATS-PHEN shows a monoclinic crystal system with a space group P21, and three symmetry-independent pairs of ATS and PHEN molecules in the asymmetric unit. Each pair features a hydrogen-bonded supramolecular synthon through O-H…N of ATS and PHEN [Figure 15(a)]. In two pairs, the carboxyl O-H donates to one N atom, while in the third pair the donor H is bifurcated between the two N atoms of the same PHEN molecule. The hydrogen atoms of the PHEN molecules form C-H…O contacts with neighbouring ATS which stabilise the packing of the dimer units [Figure 15(b)].

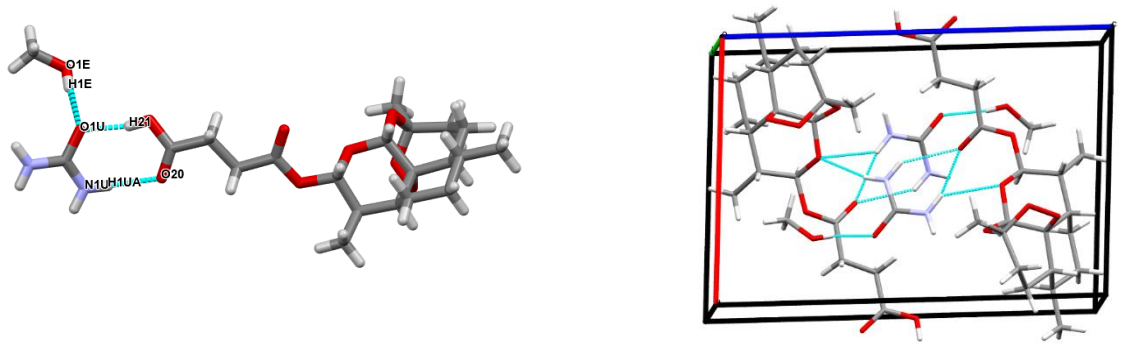


(a) (b)

Figure 15: Crystal structure packing of ATS-PHEN cocrystal: a) Supramolecular synthon linked dimer ATS-PHEN; b) Crystal packing structure

ATS-URE CH_3OH cocrystal: The crystallographic analysis of ATS-URE-CH_3OH shows a monoclinic crystal system with a space group $P2_1$. The crystal structure features the same hydrogen-bonded supramolecular synthon between ATS and URE [Figure 16(a)] as seen ATS-URE. The

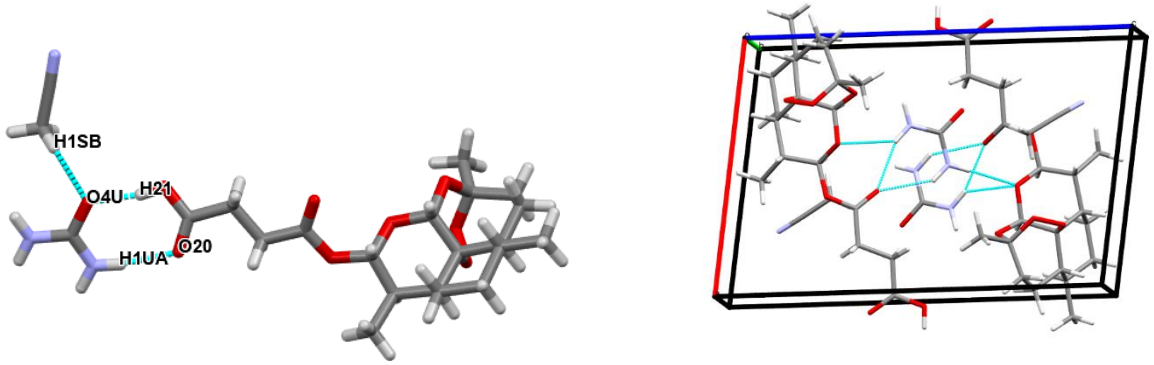
methanol molecule links this synthon through O-H…O=C hydrogen bonds with URE. Each URE molecule forms N-H…O hydrogen bonds with two further ATS molecules through their carbonyl and ether O atoms, leading to a strongly interconnected 3-D structure [Figure 16(b)].



(a) (b)

Figure 16: Crystal structure packing of ATS-URE CH_3OH cocrystal: a) Supramolecular synthon linked trimer ATS-URE CH_3OH; b) Crystal packing structure

ATS-URE C_2H_3N cocrystal: Similar to ATS-URE-CH_3OH, the acetonitrile molecule is attached to the ATS-URE dimer through C-H…OC hydrogen bonds [Figure 17(a)]. The trimer is extended through the N-H…O hydrogen bonds between URE with ATS [Figure 17(b)] to generate the final 3-D structure, which is isostructural with the methanol solvate.



(a) (b)

Figure 17: Crystal structure packing of ATS-URE C_2H_3N cocrystal: a) Supramolecular synthon linked trimer ATS-URE C_2H_3N; b) Crystal packing structure

The ORTEP drawings are shown in Table S5 of the Supporting Materials.

The simulated PXRD patterns of the crystals using the crystallographic data presented in Table S3 of the supporting materials are shown in Figure 3(a), Figure 4(a), Figure 5(a), Figure 7(a), Figure 8(a), Figure 9(a), and Figure 11(a). These figures illustrate that the peaks of the simulated patterns align well with the experimental measurements. The Bravais, Friedel, Donnay and Harker **(**BFDH) model, available in the CSD-Particle menu of CCDC Mercury software (v2023.3.0), was employed to predict the morphology of the single crystals, and the results were observed to be like the experimental single crystal shown in Table S9 of the Supporting Materials.

3.4 ΔpKa rule

ATS is a weakly acidic drug with a p*K*a of 3.9 (Table 2) and has functional groups [Figure 1(a)] with propensities to generate multicomponent adducts through hydrogen bond interaction. The

multicomponent solid forms of ATS obtained can be assessed whether they are likely to form salts or cocrystals based on the Δp*K*a rule calculated by

$$\Delta pKa = [pKa\ of\ conjugated\ acid\ of\ the\ base\ (coformer) - pKa\ of\ acid(ATS)] \quad (2)$$

If the Δp*K*a < 0 a cocrystal is formed, and when the Δp*K*a >3 a salt is expected. With a value of 0<Δp*K*a < 3, which is an intermediate region of the salt-cocrystal continuum, the multicomponent solid could be a cocrystal or a salt or a salt cocrystal adduct [25-27].

Table 2 displays the predicted p*K*a and Δp*K*a values of the coformers which have formed the multicomponent crystals of ATS. These ΔpKa values help to predict the formation of multicomponent salts or cocrystals. In combination with the analyses of FTIR spectra (Table S6 in the Supporting Materials) and structures above, it is evident that ATS has formed cocrystals with the coformers of ABA, DPE, PHEN, and URE. Based on the ΔpKa value, two forms of ATS²-DABCO should be salts. However, the structure and FTIR analysis show that there is no proton transfer for ATS²-DABCO Form 1 while for ATS²-DABCO Form 2 a partial proton transfer between the carboxyl CO bond for one of the ATS molecules could occur. Therefore, Form 1 of ATS²-DABCO is cocrystal and Form 2 is salt.

Table 2: pKa values of ATS and the coformers

Drug	Predicted (ACD/pKa Classic)		Δ pKa (ATS as an acid)	Deduction
	pKa (acidic)	pKa (basic)		
ATS	3.9 ± 0.1	No base pKa	-	-
ABA	4.9 ± 0.1	2.5 ± 0.1	-1.4	Potential cocrystal
DABCO	No acid pKa	8.2 ± 0.1	4.3	Potential salt
DPE	No acid pKa	6.1 ± 0.1	2.2	Potential cocrystal/salt
PHEN	No acid pKa	5.2 ± 0.1	1.3	Potential cocrystal/salt
URE	14.4 ± 0.5	0.1 ± 0.1	-3.8	Potential cocrystal

3.5 Degradation studies of ATS and its multicomponent crystals in solution

ATS is rapidly hydrolysed to its active metabolite DHA (α-DHA + β-DHA) because of its unstable nature in an aqueous solution [37,38]. A comparison of the degradation profiles and degradation rates of ATS and its multicomponent cocrystals in the solvent mixtures of MeOH and DDW at various ratios is given in Figure 18 and Figure S3 in the Supporting Materials and Table 3. A clear trend of decreasing ATS concentration in solution was observed as time progressed in all solvent mixtures, except for pure MeOH [Figure 18(a)], where the changes were insignificant. There is no significant difference in ATS stability in solution between ATS multicomponent crystals and the raw ATS after 24 h [Figure 18(a)].

Increasing the proportion of DDW in the solvent mixture, ATS became unstable, showing a decrease in the concentration of ATS in aqueous media in Figures 18(b), (d) and Figure S3 in the supporting materials. In the solvent mixture containing 50 % MeOH and 50 % DDW, ATS²-DABCO Form 2 and ATS²-DPE show the highest stability with 93.2% and 90.5% recovery rate of ATS concentration after 24 h in comparison with slightly lower recovery rates for ATS (86.8%), ATS-ABA (85.5%), ATS-URE (85.9%), and ATS-PHEN (87.4%), as indicated in Figure 18(b).

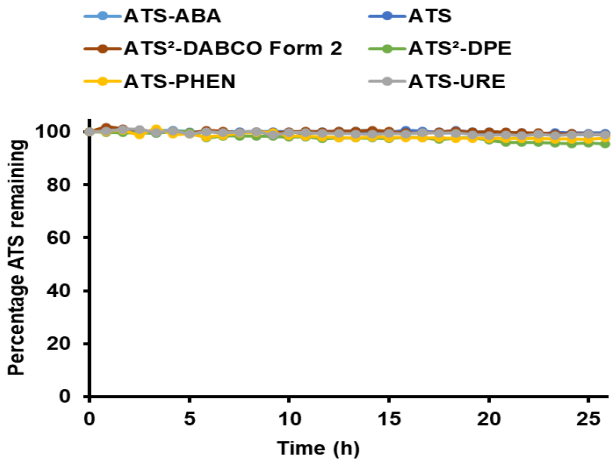
With an increase in the DDW content to 95% of DDW, as shown in Figures 18(d), a decreasing trend in the ATS concentration became apparent, and the concentration of DHA degradation product increased. Overall, the cocrystals of ATS²-DABCO Form 2 and ATS²-DPE show significantly improved ATS stability in solution compared with raw ATS and the other cocrystals of ATS-URE,

ATS-PHEN and ATS-ABA. The same trends were also observed at the other DDW contents of 80% and 90% in Figure S3 in the Supporting Materials.

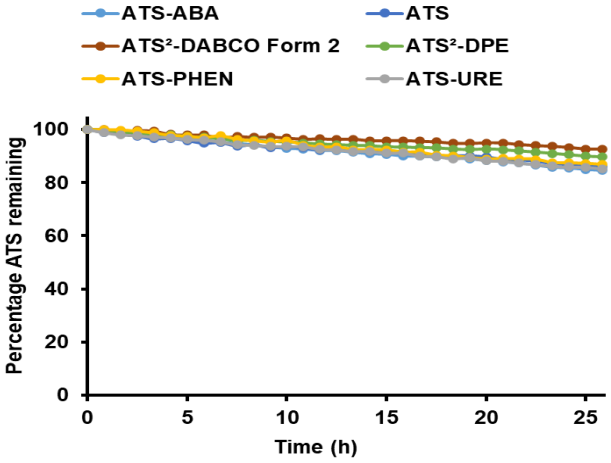
Based on the degradation tests shown in Figure 18, the degradation profiles of ATS and its multicomponent crystals follow a first-order trend. The degradation rate constant α can be obtained by Eq. (3) as

$$\%C(t) = 100 - \alpha \times t \tag{3}$$

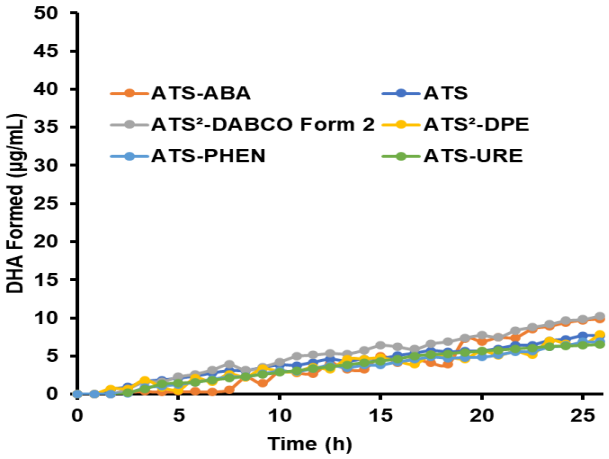
where $\%C(t)$ is the percentage of ATS remained in the solution and t is the experimental time (h). The calculated ATS degradation constants are shown in Table 3. This suggests that the stability of ATS in solution is inversely related to the water content in the system. Higher water content promotes hydrolysis, which can lead to degradation of ATS. No significant differences were observed between the degradation rates of raw ATS and ATS-URE, ATS-PHEN and ATS-ABA under the experimental conditions studied. In contrast, ATS²-DABCO Form 2 and ATS²-DPE demonstrated a lower rate of degradation compared, implying that they could be used to improve the ATS stability in solution.



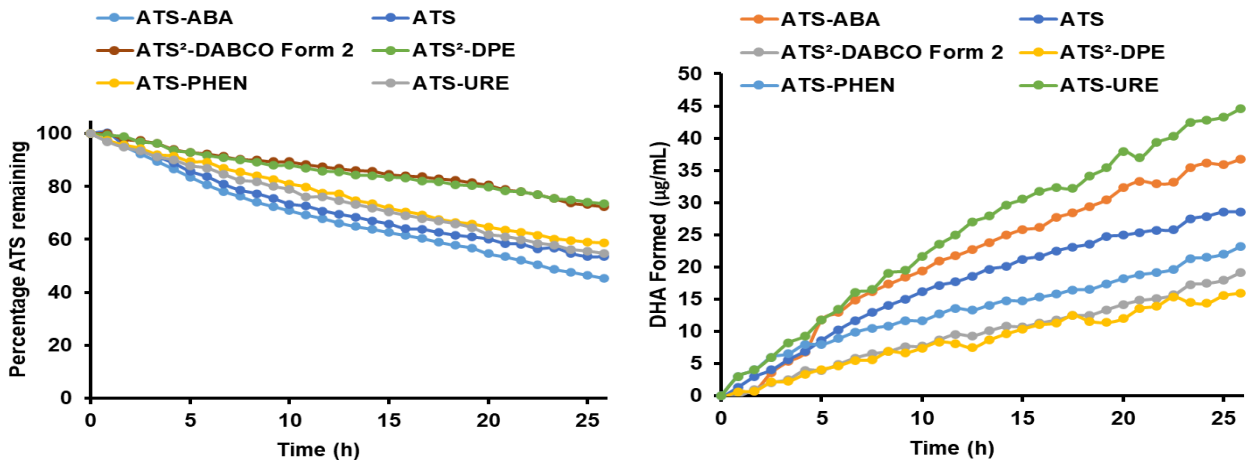
(a)



(b)



(c)



(d) (e)

Figure 18: A comparison of degradation profiles of ATS and its multicomponent crystals; a) ATS remaining in 99.8 % MeOH; b) ATS remaining in 50 % MeOH; c) DHA formed in 50 % MeOH; d) ATS remaining in 5 % MeOH; e) DHA formed in 5 % MeOH

Table 3: Degradation rate constants

	Degradation rate constant α (h^{-1})					
Solvent	**ATS-ABA**	**ATS**	**ATS²-DABCO (Form 2)**	**ATS²-DPE**	**ATS-PHEN**	**ATS-URE**
50% DWW	0.58	0.48	0.26	0.36	0.54	0.53
80% DWW	1.50	1.40	0.78	0.73	1.25	1.38
90% DWW	1.79	1.68	0.82	0.92	1.35	1.75
95% DWW	2.01	1.78	0.99	0.98	1.64	1.71

As ATS is decomposed into DHA in solution, DHA concentration curves were also obtained during the ATS measurements shown in Figure 18 and Figure S3 in the Supporting Materials. In pure MeOH solution, no noticeable components indicated degradation were detected by the HPLC measurements. In 50% DDW solution [Figure 18(c)], after 24 hours the concentrations of DHA detected, but there was no significant difference between different solids, detailed as ATS²-DABCO Form 2 (9.6 µg/mL), ATS-ABA (9.3 µg/mL), ATS (7.1 µg/mL), ATS²-DPE (6.6 µg/mL), ATS-PHEN (6.3 µg/mL), and ATS-URE (6.2 µg/mL). In 95% DDW solution [Figure 19(e)], after 24 hours the concentrations of DHA followed the following order as ATS-URE (42.8 µg/mL), ATS-ABA (36.1 µg/mL), ATS (27.8 µg/mL), ATS-PHEN (21.4 µg/mL), ATS²-DABCO Form 2 (17.4 µg/mL), and ATS²-DPE (14.3 µg/mL), indicating that ATS²-DPE is more stable in solution. These results are consistent with the ATS degradation rates obtained above, indicating that the formation of DHA varied with the solvent composition and time, with higher concentrations of DHA observed in solutions with higher proportions of DDW. Additionally, different cocrystal forms of ATS showed varying levels of DHA formation, indicating potential differences in their stability under the tested conditions.

It was also observed that the summation of the total concentrations of ATS and DHA did not match the starting ATS concentration of 100 µg/mL at time 0 (Table S10 in the Supporting Materials), implying that other degradation products may have been formed [39] or the subsequent decomposition of DHA has occurred [36].

3.6 Solid state stability studies of ATS and its multicomponent crystals under elevated conditions

The physical appearances of the test samples at the evaluated conditions of 50 ˚C and 75% of RH on different days are shown in Table 4. Overall, there is no significant difference of the appearance of each sample in the open and capped vials. The appearances of the multicomponent crystals of ATS-URE, ATS-PHEN, and ATS-ABA showed noticeable colour changes, after five days, indicating possible drug degradation. In contrast, for the raw ATS and cocrystals of ATS^2-DPE and ATS^2-DABCO Form 2, a noticeable colour change of appearance was only observed after 30 days.

Table 4: Physical appearance of samples during stability testing

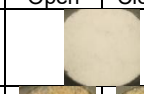
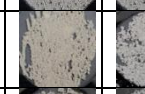
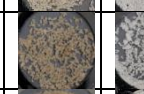
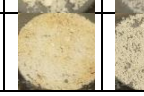
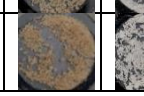
Sample/ Time	**ATS-ABA**		**Raw ATS**		**ATS^2-DABCO Form 2**		**ATS^2-DPE**		**ATS-PHEN**		**ATS-URE**	
	Open	Closed	Open	Closed	Open	Closed	Open	Closed	Open	Closed	Open	Closed
Day 0												
Day 5												
Day 10												
Day 15												
Day 30												

Figure 19 presents the ATS degradation profiles of the test samples determined by HPLC. In the closed vials, the raw ATS showed a first-order degradation rate, in which, in total 5.5 % of the drug was lost on the 30th day, as shown in Figure 19(a). A slightly higher degradation rate of the raw ATS was observed in the open vials, with 11.9% of ATS degraded on the 30th day [Figure 19(b)]. These results align well with the previous findings, where at 40 °C/75% for three months 8.1 % of ATS was lost with slight discolouration [39].

A higher-order degradation rate of ATS was observed for the multicomponent crystals of ATS-ABA, ATS^2-DABCO Form 2, ATS-PHEN or ATS-URE in both open and closed vials, in which nearly all of ATS has been lost after 30 days (Figure 20). Only ATS^2-DPE cocrystals showed a first-order degradation rate. However, it was much higher than that of the raw ATS. After 30 days, around 86.7% and 83.2% of ATS from the ATS^2-DPE cocrystals in either open or capped vials were degraded, respectively. This suggests that these multicomponent cocrystal cannot enhance the solid-state stability of ATS under the studied conditions.

The PXRD and FTIR results of each of the samples on different days of the stability tests are displayed in Table S11 in the Supporting Materials, showing mixed characteristic peaks of ATS, cocrystals and DHA. This finding is consistent with the results obtained from HPLC measurements, where both ATS in Figure 19 and DHA (Figure S4 in the Supporting Materials) were identified in solution. The DSC and TGA measurements have also been conducted, shown in Tables S12 &13 in the Supporting Materials.

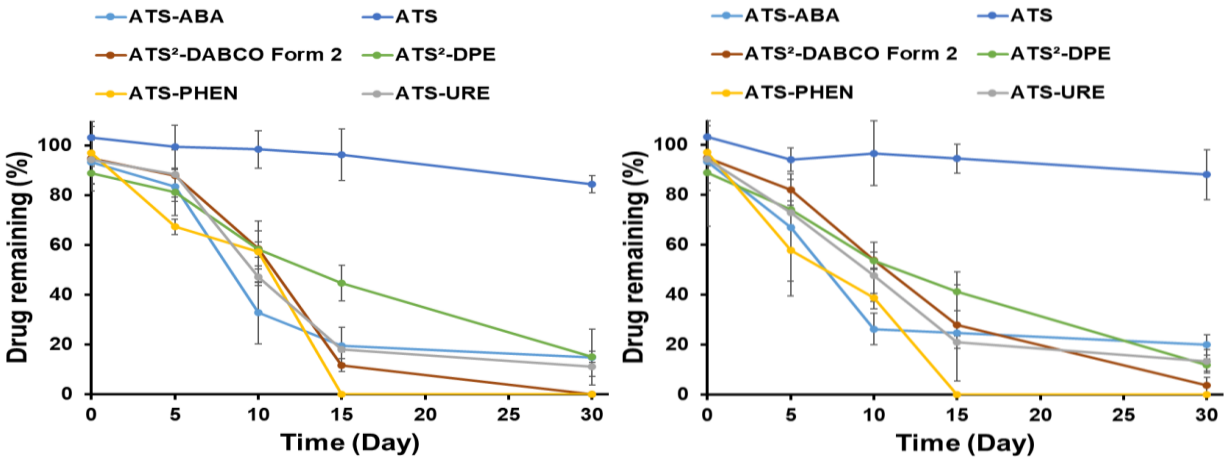


Figure 19: Solid stability tests: a) percentage of ATS remaining in a closed vial; b) percentage of ATS remaining in an open vial.

3.7 *Solubility and dissolution studies of ATS and its multicomponent crystals*

The apparent equilibrium solubility of ATS after 24 h, without considering DHA degradation, was 117.6±3.4 µg/mL, which is lower than the reported value of 296 µg/mL measured at room temperature after 1 h [40]. This lower value was attributed to the degradation of ATS to DHA and other products, as discussed above [37-39]. When including the DHA concentration in solution, the 'solubility' of ATS was increased to 360.1±5.9 µg/mL. The residues collected after the equilibrium solubility tests were the initial materials of ATS, characterised by PXRD, DSC, FTIR, and TGA, Shown in Figure S6 in the Supporting Materials.

The size of drug particles significantly influences the drug dissolution rate [41]. To minimise the impact of particle size variation on the dissolution kinetics, all the test samples were ground using a pestle and mortar and then sieved through a 60-mesh sieve (< 250 µm) before the dissolution study. The summary of particle size percentile points D10, D50, and D95 is presented in Table 5 (detailed volume percentages shown in Figure S5 in the Supporting Materials). While no significant difference was observed at D10 and D50, a slight variation was noticed at D95, potentially attributed to a few outliers during measurement. The mean particle sizes of the powder samples also indicated only a small variation among them. Thus, variation in dissolution can be attributed to crystal packing arrangements as opposed to the particle sizes of the powders.

Table 5: Summary of D10, D50, and D95 particle size percentiles

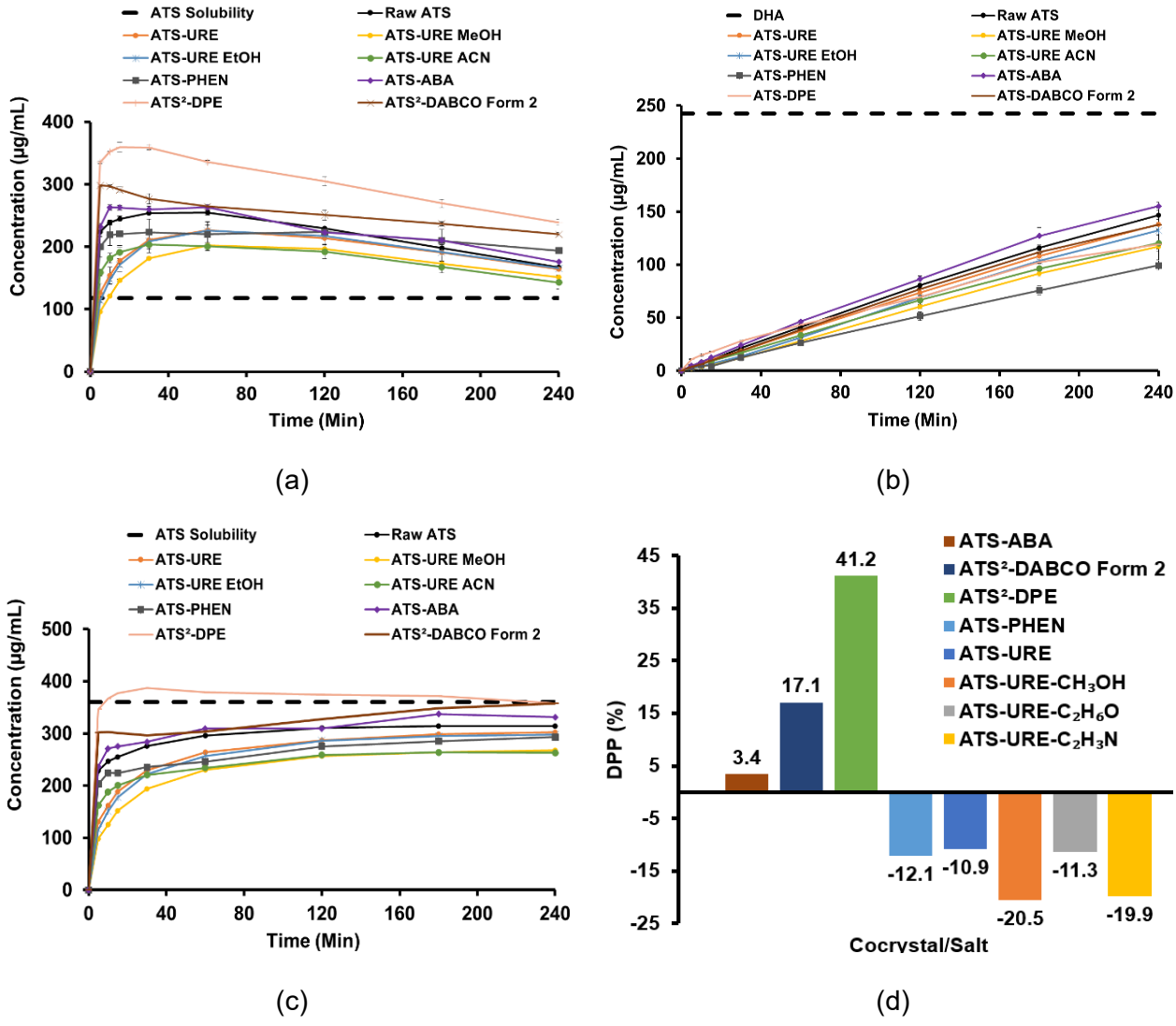
Percentiles	ATS-ABA (µm)	ATS (µm)	ATS²-DABCO Form 2 (µm)	ATS²-DPE (µm)	ATS-PHEN (µm)	ATS-URE (µm)	ATS-URE CH_3OH (µm)	ATS-URE C_2H_6O (µm)	ATS-URE C_2H_3N (µm)
D10	37.04	41.94	22.26	27.98	56.42	38.11	22.95	44.44	32.19
D50	141.2	114.4	75.92	131.1	154.8	151.5	93.98	142.8	134.1
D95	306.9	220.6	228.3	320.8	325.3	323.9	254.4	293	292.3
Mean (µm)	150.3	118.4	95.5	140.3	168.9	154.8	108.1	148.5	137.8

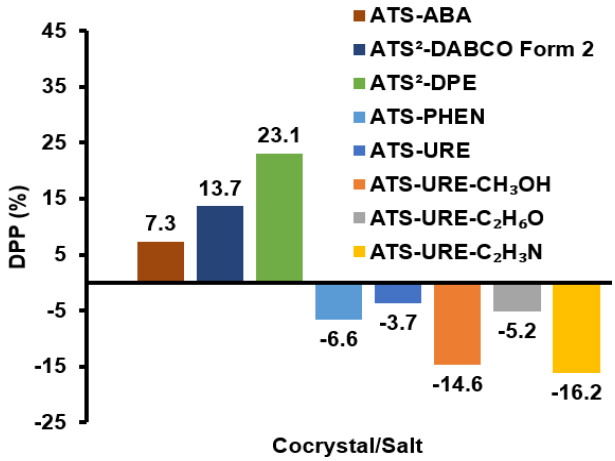
The dissolution profiles of ATS and its multicomponent cocrystals are shown in Figure 20. Figure 20(a) presents the dissolution profile without considering the DHA degradation of ATS in solution. The dissolution profile of ATS exceeded the equilibrium solubility of 117.62 µg/mL after 5 minutes. Similar findings were observed with all cocrystals studied, except for ATS-URE MeOH and ATS-URE EtOH, which remained below the apparent equilibrium solubility of ATS at 96.6 and 113.2 µg/mL, respectively, after 5 min. ATS²-DPE released a maximum of 359.6 µg/mL at 15 min, which decreased but remained above the ATS concentration curve. Similarly, ATS²-DABCO Form 2 released a maximum of 298.3 µg/mL at 5 minutes, decreasing slowly but remaining above the ATS dissolution profile. ATS-ABA released a maximum of 263.2 µg/mL at 60 min. The DPP values in Eq.

(1) [Figure 20(d)] indicates that ATS^2-DPE, ATS^2-DABCO form 2, and ATS-ABA improved ATS release performance by 41.2%, 17.1%, and 3.4%, respectively. ATS-URE, ATS-URE MeOH, ATS-URE EtOH, ATS-URE ACN, and ATS-PHEN had negative DPP values shown in Figure 20(d), indicating that it could be difficult to select them for performance improvement in the formulation.

As mentioned above, part of ATS was degraded into DHA in aqueous solution. The concentration profiles of DHA in solution are shown in Figure 20(b), showing a linear increase in the DHA concentration with time. This concords with the degradation results in section 3.5, suggesting a first-order hydrolysis of ATS into DHA. When the DHA concentration was added to the ATS dissolution profile [Figure 20(c)], the DPP in Figure 20(e) shows that ATS^2-DPE, ATS^2-DABCO Form 2 and ATS-ABA improved the ATS dissolution by 23.1, 13.7 and 7.3 %, respectively. In particular, a maximum concentration of ATS released from ATS^2-DPE can reach 386.8 μg/mL at 30 min, which is significantly higher than the raw ATS and other multicomponent crystals.

The residues recovered following the dissolution of the raw ATS were the starting materials of ATS, confirmed by PXRD, DSC, TGA, and FTIR results (Figure S6 in the Supporting Materials). Phase transformations to ATS were observed in the residues collected after the dissolution of ATS cocrystals of ATS-URE, ATS-URE-CH_3OH, ATS-URE-C_2H_6O, ATS-URE-C_2H_3N, and ATS-ABA, confirmed by PXRD results shown in Figures S7-12 in the supporting materials. As ATS^2-DPE and ATS^2-DABCO Form 2 were completely dissolved in the dissolution medium, PXRD measurement cannot be conducted.





(e)

Figure 20: The dissolution profile of ATS and cocrystals: a) ATS concentration in solution; b) DHA concentration in solution c) sum of ATS and αβ-DHA in solution; d) DPP of ATS in solution; e) DPP of ATS + αβ-DHA in solution

4. Conclusion

In this work, novel multicomponent crystal forms of ATS with ABA, DABCO, DPE, PHEN and URE are reported. Based on the Δp*K*a rule, FTIR results and structure analyses, all of them are cocrystals except DABCO. Additionally, ATS-URE cocrystals can be crystallised as different solvate forms, including MeOH, EtOH, and ACN. Interestingly, two forms of ATS^2-DABCO have been discovered, i.e., Form 1 is cocrystal and Form 2 is salt. The crystal structures of these multicomponent ATS crystal forms were determined by SXRD and characterised by PXRD, FTIR and different thermal analytical techniques (i.e., DSC, TGA and HSM). It has been shown that some of the multicomponent crystals of ATS can significantly improve the in vitro dissolution performance of ATS and its stability in solution. For example, ATS^2-DPE can increase the dissolution performance by 41.2% with a lower rate of degradation in comparison with the raw ATS, indicating it could be employed in dosage forms as oral reconstituted suspensions and dispersible tablets in malaria therapy. Unfortunately, the solid-state stability study shows that these multicomponent cocrystals do not exhibit better stability than the raw ATS under the conditions studied. In conclusion, the discovery of more multicomponent crystal forms of ATS with improved physiochemical properties (e.g., solubility and/or stability) could help to enhance its therapeutic efficacy, minimising the threat and impact of antimalarial drug resistance and contributing to the WHO global technical strategy for malaria.

Notes

The authors declare no competing financial interest.

Data availability

Data supporting this article have been included as part of the Supporting Materials. Crystal structures have been deposited in the Cambridge Structural Database (CSD) with CCDC deposition numbers 2427253 – 2427258.

Acknowledgements

The authors would like thank University of East Anglia for providing access to the diffractometer for SXRD measurements.

References

1 World-Health-Organization. World malaria report 2019. *WHO Geneva: ISBN 978-92-4-156572-1* (2019).
2 Adebayo, J. O. *et al.* Enhancing the antimalarial activity of artesunate. *Parasitology Research* **119**, 2749-2764 (2020). https://doi.org/10.1007/s00436-020-06786-1
3 Wang, J. *et al.* Artemisinin, the magic drug discovered from traditional Chinese medicine. *Engineering* **5**, 32-39 (2019).
4 Desrosiers, M. R., Mittleman, A. & Weathers, P. J. Dried leaf Artemisia annua improves bioavailability of artemisinin via cytochrome P450 inhibition and enhances artemisinin efficacy downstream. *Biomolecules* **10**, 254 (2020).
5 Meng, H. *et al.* Nanocapsules based on mPEGylated artesunate prodrug and its cytotoxicity. *Colloids and Surfaces B: Biointerfaces* **115**, 164-169 (2014).
6 Ruwizhi, N., Maseko, R. B. & Aderibigbe, B. A. Recent Advances in the Therapeutic Efficacy of Artesunate. *Pharmaceutics* **14**, 504 (2022).
7 delMoral-Sanchez, J.-M., Gonzalez-Alvarez, I., Gonzalez-Alvarez, M., Navarro, A. & Bermejo, M. Classification of WHO essential oral medicines for children applying a provisional pediatric biopharmaceutics classification system. *Pharmaceutics* **11**, 567 (2019).
8 Badawi, A. & Geneidi, A. S. Enhancing dissolution of artesunate from immediate release tablets using a green granulation technique. *Archives of Pharmaceutical Sciences Ain Shams University* **3**, 55-77 (2019).
9 Setyawan, D., Kusuma, N. & Sari, R. Solubility, dissolution test and antimalarial activity of artesunate nicotinamide co-crystal prepared by solvent evaporation and slurry methods. *Asian Journal of Pharmaceutical and Clinical Research* **8**, 164-166 (2015).
10 Aderibigbe, B. A. Design of Drug Delivery Systems Containing Artemisinin and Its Derivatives. *Molecules* **22**, 323 (2017).
11 Agnihotri, J., Sobhna, S. & Papiya, B. Formal chemical stability analysis and solubility analysis of artesunate and hydroxychloroquinine for development of parenteral dosage form. *Journal of Pharmacy Research* **6**, 117-122 (2013). https://doi.org/https://doi.org/10.1016/j.jopr.2012.11.025
12 Agnihotri, J., Singh, S. & Bigonia, P. Formal chemical stability analysis and solubility analysis of artesunate and hydroxychloroquinine for development of parenteral dosage form. *journal of pharmacy research* **6**, 117-122 (2013).
13 Nguyen, H. T., Tran, T. H., Kim, J. O., Yong, C. S. & Nguyen, C. N. Enhancing the in vitro anti-cancer efficacy of artesunate by loading into poly-D, L-lactide-co-glycolide (PLGA) nanoparticles. *Archives of pharmacal research* **38**, 716-724 (2015).
14 Jiang, R.-j. *et al.* Synthesis, characterization, and in vitro evaluation of artesunate-β-cyclodextrin conjugates as novel anti-cancer prodrugs. *Carbohydrate Research* **400**, 19-25 (2014). https://doi.org/https://doi.org/10.1016/j.carres.2014.08.018
15 Ismail, M., Du, Y., Ling, L. & Li, X. Artesunate-heparin conjugate based nanocapsules with improved pharmacokinetics to combat malaria. *International Journal of Pharmaceutics* **562**, 162-171 (2019). https://doi.org/https://doi.org/10.1016/j.ijpharm.2019.03.031
16 Agbo, C. P. *et al.* Intranasal artesunate-loaded nanostructured lipid carriers: A convenient alternative to parenteral formulations for the treatment of severe and cerebral malaria. *Journal of Controlled Release* **334**, 224-236 (2021). https://doi.org/https://doi.org/10.1016/j.jconrel.2021.04.020
17 Qiao, N. *et al.* Pharmaceutical cocrystals: An overview. *International Journal of Pharmaceutics* **419**, 1-11 (2011). https://doi.org/http://dx.doi.org/10.1016/j.ijpharm.2011.07.037
18 Elder, D. P., Holm, R. & Diego, H. L. d. Use of pharmaceutical salts and cocrystals to address the issue of poor solubility. *International Journal of Pharmaceutics* **453**, 88-100 (2013). https://doi.org/https://doi.org/10.1016/j.ijpharm.2012.11.028
19 Xue, Z.-H., Huang, B., Li, H. & Yan, Q.-L. Nitramine-Based Energetic Cocrystals with Improved Stability and Controlled Reactivity. *Crystal Growth & Design* **20**, 8124-8147 (2020). https://doi.org/10.1021/acs.cgd.0c01122

20 Svärd, M., Ahuja, D. & Rasmuson, Å. C. Calorimetric Determination of Cocrystal Thermodynamic Stability: Sulfamethazine–Salicylic Acid Case Study. *Crystal Growth & Design* **20**, 4243-4251 (2020). https://doi.org/10.1021/acs.cgd.9b01253
21 Yang, D. *et al.* Solubility and Stability Advantages of a New Cocrystal of Berberine Chloride with Fumaric Acid. *ACS Omega* **5**, 8283-8292 (2020). https://doi.org/10.1021/acsomega.0c00692
22 Jiang, Q., Hirsh, D. A., Tu, Y. & Luo, L. Multicomponent crystals of an artemisinin derivative and cinchona alkaloids for use as antimalarial drugs. *CrystEngComm* **23**, 6843-6847 (2021). https://doi.org/10.1039/D1CE00974E
23 LUO, B. *et al.* Synthesis, Characterization and Antibacterial Activities Study of a Pharmaceutical Cocrystal of Artesunate and 4,4′-Bipyridine. *CHINESE JOURNAL OF STRUCTURAL CHEMISTRY* **39**, 1633-1638 (2020).
24 Setyawan, D. W. I., Sari, R., Yusuf, H. & Primaharinastiti, R. Preparation and characterization of artesunate-nicotinamide cocrystal by solvent evaporation and slurry method. *Asian Journal of Pharmaceutical and Clinical Research* **7**, 62-65 (2014).
25 Cruz-Cabeza, A. J. Acid–base crystalline complexes and the pKa rule. *CrystEngComm* **14**, 6362-6365 (2012). https://doi.org/10.1039/C2CE26055G
26 Childs, S. L., Stahly, G. P. & Park, A. The Salt−Cocrystal Continuum: The Influence of Crystal Structure on Ionization State. *Molecular Pharmaceutics* **4**, 323-338 (2007). https://doi.org/10.1021/mp0601345
27 Aakeröy, C. B., Fasulo, M. E. & Desper, J. Cocrystal or Salt: Does It Really Matter? *Molecular Pharmaceutics* **4**, 317-322 (2007). https://doi.org/10.1021/mp060126o
28 Caine, B. A. *et al.* Aqueous pK(a) prediction for tautomerizable compounds using equilibrium bond lengths. *Commun Chem* **3**, 21 (2020). https://doi.org/10.1038/s42004-020-0264-7
29 ACD/labs. https://www.acdlabs.com/products/percepta-platform/physchem-suite/pka/#pka_calculations.
30 Guo, M. *et al.* Insight into Flufenamic Acid Cocrystal Dissolution in the Presence of a Polymer in Solution: from Single Crystal to Powder Dissolution. *Molecular Pharmaceutics* **14**, 4583-4596 (2017). https://doi.org/10.1021/acs.molpharmaceut.7b00712
31 Dolomanov, O. V., Bourhis, L. J., Gildea, R. J., Howard, J. A. K. & Puschmann, H. OLEX2: a complete structure solution, refinement and analysis program. *Journal of Applied Crystallography* **42**, 339-341 (2009). https://doi.org/doi:10.1107/S0021889808042726
32 Sheldrick, G. SHELXT - Integrated space-group and crystal-structure determination. *Acta Crystallographica Section A* **71**, 3-8 (2015). https://doi.org/doi:10.1107/S2053273314026370
33 Sheldrick, G. Crystal structure refinement with SHELXL. *Acta Crystallographica Section C* **71**, 3-8 (2015). https://doi.org/doi:10.1107/S2053229614024218
34 Pongsamart, K., Limwikrant, W., Ruktanonchai, U. R., Charoenthai, N. & Puttipipatkhachorn, S. Preparation, characterization and antimalarial activity of dihydroartemisinin / β-cyclodextrin spray-dried powder. *Journal of Drug Delivery Science and Technology* **73**, 103434 (2022). https://doi.org/https://doi.org/10.1016/j.jddst.2022.103434
35 IP. Tests and general requirements for dosage forms quality specifications for Pharmaceutical Substances and tablets. **5**, 222 (2003).
36 Haynes, R. K. *et al.* Artesunate and Dihydroartemisinin (DHA): Unusual Decomposition Products Formed under Mild Conditions and Comments on the Fitness of DHA as an Antimalarial Drug. *ChemMedChem* **2**, 1448-1463 (2007). https://doi.org/https://doi.org/10.1002/cmdc.200700064
37 Gashe, F., Wynendaele, E., De Spiegeleer, B. & Suleman, S. Degradation kinetics of artesunate for the development of an ex-tempore intravenous injection. *Malaria Journal* **21**, 256 (2022). https://doi.org/10.1186/s12936-022-04278-4
38 Gaudin, K. *et al.* Stability of artesunate in pharmaceutical solvents. *Journal of Pharmaceutical and Biomedical Analysis* **43**, 1019-1024 (2007). https://doi.org/https://doi.org/10.1016/j.jpba.2006.09.039
39 Bezuidenhout, J. W., Aucamp, M., Stieger, N., Liebenberg, W. & Haynes, R. K. Assessment of Thermal and Hydrolytic Stabilities and Aqueous Solubility of Artesunate for Formulation Studies. *AAPS PharmSciTech* **24**, 33 (2023). https://doi.org/10.1208/s12249-022-02490-8

40 Kauss, T. *et al.* Fixed artesunate–amodiaquine combined pre-formulation study for the treatment of malaria. *International Journal of Pharmaceutics* **395**, 198-204 (2010). https://doi.org/https://doi.org/10.1016/j.ijpharm.2010.05.038

41 Shi, K. & Li, M. Optimisation of Pharmaceutical Cocrystal Dissolution Performance through a Synergistic Precipitation Inhibition. *Pharm Res* **40**, 2051-2069 (2023). https://doi.org/10.1007/s11095-023-03532-x